Tietze, K., Ritter, O., Egbert, G. D. (2015): 3-D joint inversion of the magnetotelluric phase tensor and vertical magnetic transfer functions. - *Geophysical Journal International*, *203*, 2, p. 1128-1148.

DOI: http://doi.org/10.1093/gji/ggv347

Geophysical Journal International

Geophys. J. Int. (2015) **203,** 1128–1148 doi: 10.1093/gji/ggv347

GJI Geomagnetism, rock magnetism and palaeomagnetism

3-D joint inversion of the magnetotelluric phase tensor and vertical magnetic transfer functions

Kristina Tietze,[1] Oliver Ritter[1] and Gary D. Egbert[2]

[1]*German Research Centre for Geosciences GFZ, Potsdam, Germany. E-mail: ktietze@gfz-potsdam.de*

[2]*College of Earth, Ocean, and Atmospheric Sciences, Oregon State University, Corvallis, OR, USA*

Accepted 2015 August 17. Received 2015 August 13; in original form 2014 May 1

SUMMARY

With advancing computational resources, 3-D inversion techniques have become feasible in recent years and are now a more widely used tool for magnetotelluric (MT) data interpretation. Galvanic distortion caused by small-scale near-surface inhomogeneities remains an obstacle for 3-D MT inversion which so far has experienced little attention. If not considered properly, the effect on 3-D inversion can be immense and result in erroneous subsurface models and interpretations. To tackle the problem we implemented inversion of the distortion-free phase tensor into the ModEM inversion package. The dimensionless phase tensor components describe only variations of the conductivity structure. When inverting these data, particular care has to be taken of the conductivity structure in the *a priori* model, which provides the reference frame when transferring the information from phase tensors into absolute conductivity values. Our results obtained with synthetic data show that phase tensor inversion can recover the regional conductivity structure in presence of galvanic distortion if the *a priori* model provides a reasonable assumption for the regional resistivity average. Joint inversion of phase tensor data and vertical magnetic transfer functions improves recovery of the absolute resistivity structure and is less dependent on the prior model. We also used phase tensor inversion for a data set of more than 250 MT sites from the central San Andreas fault, California, where a number of sites showed significant galvanic distortion. We find the regional structure of the phase tensor inversion results compatible with previously obtained models from impedance inversion. In the vicinity of distorted sites, phase tensor inversion models exhibit more homogeneous/smoother conductivity structures.

Key words: Inverse theory; Magnetotellurics; Geomagnetic induction; Continental margins: transform; North America.

1 INTRODUCTION

Interpretation of magnetotelluric (MT) data by 3-D inversion has become feasible and a widely used technique in recent years. Though galvanic distortion has long been recognized as an obstacle for MT interpretation and been subject of much research, it has only recently experienced significant attention in the context of 3-D inversion. If galvanic distortion is not appropriately considered in MT inversion, resulting subsurface images of regional structures can be misleading and subsequent interpretation erroneous.

Galvanic distortion of MT impedance responses is caused by ubiquitous near-surface inhomogeneities (galvanic scatterers) of dimensions below the resolution scale of the MT experiment, that is below the inductive scale length of the lowest period (e.g. Bahr 1988; Jiracek 1990; Bibby *et al.* 2005). The degree of galvanic distortion varies from site to site and depends on the survey area. It is usually lower in sedimentary basins and high above old, high-resistive material, that is on cratons (Sasaki & Meju 2006, and references therein). Galvanic distortion of the MT responses is commonly described by a real, frequency-independent tensor $\mathbf{C}$ which links the observed impedance tensor $\mathbf{Z}$ to a regional MT response $\mathbf{Z}_R$ which would be measured in absence of any near-surface inhomogeneities (e.g. Bahr 1988):

$$\mathbf{Z}(\omega) = \mathbf{C} \cdot \mathbf{Z}_R(\omega), \quad \mathbf{C} = \begin{pmatrix} c_{xx} & c_{xy} \\ c_{yx} & c_{yy} \end{pmatrix}, \tag{1a}$$

$$\begin{pmatrix} Z_{xx} & Z_{xy} \\ Z_{yx} & Z_{yy} \end{pmatrix} = \begin{pmatrix} c_{xx}Z^R_{xx} + c_{xy}Z^R_{yx} & c_{xx}Z^R_{xy} + c_{xy}Z^R_{yy} \\ c_{yx}Z^R_{xx} + c_{yy}Z^R_{yx} & c_{yx}Z^R_{xy} + c_{yy}Z^R_{yy} \end{pmatrix}; \tag{1b}$$

ω indicates frequency dependence. In the general 3-D case the observed impedance tensor elements Z_{ij} will be a mixture of two elements of the regional impedance $\mathbf{Z}_R$ (eq. 1b). As a consequence, both

the amplitude and the phase of the observed complex impedances may differ from the regional (undistorted) values (see also Jones 2011). With a 1-D situation or a 2-D subsurface where the coordinate system is aligned with the geo-electric strike direction, the diagonal elements of $\boldsymbol{Z}_{\mathrm{R}}$ vanish. In this case, phases of the off-diagonal impedance elements, which are used for 1-D and 2-D interpretation, are preserved, and only the impedance magnitudes, that is the apparent resistivities, are biased. Hence, any galvanic distortion of the measured off-diagonal components will be expressed as an offset of the log-apparent-resistivity versus period curves, known as static shift.

Effective strategies for handling galvanically distorted MT data have been developed mainly for 2-D inversion and mostly consider the static shift case; comprehensive reviews of these methods are given in for example Jiracek (1990) and Jones (2011). For 3-D inversion various approaches have been suggested and used to handle galvanic distortion. A number of workers explicitly assume that 3-D inversion solves the problem by adding compensating structures to the surface layers (Newman *et al.* 2008; Farquharson & Craven 2009; Xiao *et al.* 2010; Kelbert *et al.* 2012). However, discretization of the subsurface with sufficiently fine detail which allows for modelling of such small-scale heterogeneities (e.g. on metre-scale) is often impractical in 3-D as the number of model parameters very rapidly exceeds manageable sizes. If the lateral model mesh discretization is coarse relative to inter-site distances or to skin depths associated with the highest frequencies used in inversion, it is unclear how successful this approach will be. Heise *et al.* (2008, 2010), Hill *et al.* (2009), Ingham *et al.* (2009) remove distortion from the transfer functions by a tensor decomposition method described by Bibby *et al.* (2005), arguing that the top-layer cells of the model are too large to properly account for galvanic distortion (Heise *et al.* 2010). Árnason *et al.* (2010) and Cumming & Mackie (2010) attempt to correct static shift of impedances prior to inversion using time-domain electromagnetic measurements. 3-D inversion codes solving for static shift as an additional, independent parameter have been demonstrated for synthetic data (Sasaki 2004; Sasaki & Meju 2006). Recently, Avdeeva *et al.* (2015) presented promising results using a 3-D inversion solving simultaneously for the subsurface conductivity structure and full distortion matrix.

Koyama (2009) proposed inversion of the phase tensor (PT; Caldwell *et al.* 2004) for galvanically distorted data sets. In a Cartesian coordinate system (x_1, x_2, x_3) with x_1, x_2 parallel to surface and x_3 positive downwards, the phase tensor Φ is defined in the following way (Caldwell *et al.* 2004):

$$\begin{aligned}\boldsymbol{\Phi} &= \mathbf{X}^{-1}\mathbf{Y} \\ &= \frac{1}{\det\,\mathbf{X}}\begin{pmatrix} X_{22}Y_{11} - X_{12}Y_{21} & X_{22}Y_{12} - X_{12}Y_{22} \\ X_{11}Y_{21} - X_{21}Y_{11} & X_{11}Y_{22} - X_{21}Y_{12}\end{pmatrix},\end{aligned} \tag{2}$$

where X and Y are the real and imaginary part of the MT impedance $\mathbf{Z} = \mathbf{X} + i\mathbf{Y}$. The phase tensor is derived from the observed impedance, but is unaffected by galvanic distortion (Caldwell *et al.* 2004). Its invariants provide distortion-free information about the dimensionality of the underlying conductivity structure, which can be obtained directly from the observed distorted data. A detailed review of the phase tensor and its potential for MT data interpretation is given in Booker (2013).

Analogous to vertical magnetic transfer functions (VTFs), the dimensionless phase tensor components describe mainly variations of the conductivity structure (Caldwell *et al.* 2004). Thus, when inverting these data, particular care has to be taken of the conductivity structure in the *a priori* model, which provides the reference frame when transferring the information from phase tensors into absolute conductivity values (*cf.* Patro *et al.* 2013). We implemented 3-D inversion of the PT into the ModEM software package (Egbert & Kelbert 2012; Kelbert *et al.* 2014). Our PT inversion approach is similar to that of Patro *et al.* (2013) who appended inversion of the phase tensor to the WSINV3DMT code of Siripunvaraporn *et al.* (2005). Moreover, ModEM allows joint inversion of PT data and VTFs which are also free of galvanic distortion. In the following, we will present PT inversion with ModEM and results from joint PT and VTF inversion of synthetic and real data.

2 METHODOLOGY

2.1 Modifications to the ModEM software package

The inversion algorithm of the ModEM software package (Egbert & Kelbert 2012; Kelbert *et al.* 2014) is based on a standard minimum-structure non-linear conjugate gradients (NLCG) algorithm. The program is parallelized to enable concurrent computations of different frequencies and source polarizations (Meqbel 2009). Concept and implementation of the ModEM software package are discussed in detail in Egbert & Kelbert (2012), Kelbert *et al.* (2014) and Meqbel (2009). Hence, we only describe modifications made to the 3-D MT inversion scheme.

Primarily, it was necessary to adopt the sensitivity calculation of ModEM to facilitate inversion of the phase tensor. The sensitivities describe changes of the observed data with respect to changes in the resistivity model structure; they are calculated at each NLCG iteration as part of the model update. As the phase tensor is derived from the impedance tensor, we used the sensitivity of the impedances which are already calculated in ModEM to obtain the respective sensitivities.

We invert the phase tensor in terms of its four real-valued tensor components Φ_{ij}. The sensitivity of the phase tensor $\boldsymbol{\Phi}$ with respect to the solution of the electric fields on the model grid $\mathbf{e}$ can be derived using the chain rule

$$\frac{\partial\boldsymbol{\Phi}}{\partial\mathbf{e}} = \frac{\partial\boldsymbol{\Phi}}{\partial\mathbf{Z}}\frac{\partial\mathbf{Z}}{\partial\mathbf{e}} = \frac{\partial\boldsymbol{\Phi}}{\partial X}\frac{\partial\mathbf{X}}{\partial\mathbf{e}} + \frac{\partial\boldsymbol{\Phi}}{\partial\mathbf{Y}}\frac{\partial\mathbf{Y}}{\partial\mathbf{e}}. \tag{3}$$

Eq. (3) means that sensitivities for phase tensor components can be obtained by a linear combination of the impedance sensitivities weighted by the derivatives of the phase tensor elements with respect to the (real and imaginary parts of the) impedance tensor elements. For each PT component Φ_{ij}, the term

$$\frac{\partial\boldsymbol{\Phi}_{\mathrm{ij}}}{\partial\mathbf{e}} = \frac{\partial\boldsymbol{\Phi}_{\mathrm{ij}}}{\partial\mathbf{Z}}\frac{\partial\mathbf{Z}}{\partial\mathbf{e}} = \begin{pmatrix} \frac{\partial\Phi_{\mathrm{ij}}}{\partial X_{11}} \\ \frac{\partial\Phi_{\mathrm{ij}}}{\partial X_{12}} \\ \vdots \\ \frac{\partial\Phi_{\mathrm{ij}}}{\partial Y_{22}} \end{pmatrix} \cdot \begin{pmatrix} \frac{\partial X_{11}}{\partial\mathbf{e}} \\ \frac{\partial X_{12}}{\partial\mathbf{e}} \\ \vdots \\ \frac{\partial Y_{22}}{\partial\mathbf{e}} \end{pmatrix} \tag{4}$$

is evaluated, as in Patro *et al.* (2013). A sketch of the approach, with an explicit expression for one element of the phase tensor, is given in the Appendix. These expressions are then used to modify data functional modules of ModEM, to allow evaluation of sensitivities for this new data type, as outlined in Egbert & Kelbert (2012) and Kelbert *et al.* (2014).

Our implementation in ModEM is similar to that of Patro *et al.* (2013) in the WSINV3DMT code. The main differences arise from differences in the underlying inversion codes. In particular, ModEM was designed to simplify addition of new data types, in a manner that allows simultaneous inversion of arbitrary combinations, for example impedance, VTFs, and with our modifications phase tensors, can be inverted separately or in combination. In the following, we make use of this capability to compare results of impedance, PT and PT + VTF inversion using both synthetic data and field data from a large, and already well-studied, 3-D array with more than 250 MT sites.

2.2 Data errors for phase tensor inversion

The phase tensor is a dimensionless quantity. In general, the elements of the phase tensor are not a function of the impedance phases, although the name may evoke this association. Above a homogeneous half-space the PT is identical to the identity matrix. In layered 1-D and 2-D situations with the x-axis of the coordinate system parallel to strike, the phase tensor is diagonal and its components Φxx and Φyy are the tangents of the conventional Zxy and Zyx impedance phases, respectively (Caldwell *et al.* 2004). As the relation of the amplitude of a PT element to changes in subsurface resistivity (or impedance phases) is highly non-linear, a constant error as it is often used for VTF data and MT phases (e.g. Becken *et al.* 2011; Weckmann *et al.* 2012), is not appropriate. Considering 1-D and 2-D cases where $\Phi_{ii} = \tan(\varphi_{ij})$ and using $\Delta \tan\varphi = (1 + \Delta \tan^2\varphi)\Delta\varphi$, linearized error propagation shows that an error $\Delta\varphi$ in the phase scales to $\Delta\Phi_{ii} = (1 + \Delta\Phi_{ii}^2)\Delta\varphi$, in Φ_{ii}. That is, if the error level in phase is constant, the error level in Φ_{ii} would be proportional to ${\Phi^2}_{ii}$ plus some constant.

For field data, Patro *et al.* (2013) estimated uncertainties for the phase tensor elements from impedance variances by applying the delta method. This procedure assumes that the variances of the impedance tensor elements obtained from time-series processing are well defined. For phase tensor parameters such as the skew value Booker (2013) pointed out that not only the variances but also the covariances of the impedance elements have significant influence when estimating uncertainties using the delta method and need to be considered; for the phase tensor elements itself the effect may not be as severe but should probably be considered as well. Moreover, if the impedance tensor elements are manipulated later, a sound estimation of the corresponding variances may be challenging. If, for example, impedances are rotated, the co-variances of the impedance tensor elements are required to estimate impedance variances for the rotated coordinate system. In practice, co-variances are often neglected and variances for the rotated data are simply estimated by multiplying a 2 × 2 'variance matrix' consisting of the impedance element variances with a rotation operator. However, such simplifying assumptions can lead to misleading inversion results (see Tietze & Ritter 2013). Furthermore, for inversion, statistically derived data errors are often discarded in favour of error bounds proportional to the amplitude of impedance tensor elements.

In view of the above considerations and to avoid over-simplifying assumptions, we chose to consider phase tensor data uncertainties independently of any other data type. We define the errors for phase tensor data relative to the amplitude of the PT elements, for example 3 per cent of abs(Φ_{ij}), in combination with a floor in the range of 0.03 to avoid very small error values close or equal to zero both for synthetic and field data.

3 SYNTHETIC EXAMPLE

3.1 Data sets and 3-D inversion setup

The synthetic data set was generated from the Oblique Conductor (OC) model displayed in Fig. 1(a), which is based on a model of Ledo (2006). The model comprises a regional 2-D resistivity structure formed by two half-layers of 50 and 500 Ωm between 0.1 and 70.8 km depth; above and below model resistivities were set to 100 Ωm. In the central domain, the OC model comprises a conductive block (5 Ωm) of 30 × 9 × 9 km^3 located with its top at 2.56 km depth. The major axis of the block is rotated 45° from the strike direction of the regional 2-D resistivity structure and crosses the contact plane of the two half-layers. For forward modelling, the model structure was discretized horizontally by a 1 km × 1 km mesh beneath the station array. Horizontally, 24 planes in each direction pad the central domain with cell widths increasing by a factor of 1.2. In the vertical direction, the thickness of the first layer is 20 m; subsequent layer thicknesses increase by a factor of 1.2. The conductive block is located in layers 19–26.

Phase tensor (PT), impedance (Z) and VTF data were calculated for a 10 × 10-site array with 4 km site spacing which covers the OC structure. We used 16 periods between 0.01 and 1000 s. The conductive block influences data between 0.1 and 100 s; the strongest 3-D effects are observed between 1 and 100 s. For these periods, the direction of PT major axes and induction vectors change rapidly across the conductive block and PT β-values exceed ±3° in wide parts of the station array (Figs 1b–d). Prior to inversion 3 per cent Gaussian noise was added to the corresponding impedance and phase tensor elements; for VTF data noise is distributed normally around zero with a standard deviation of 0.02.

For subsequent 3-D inversion of the OC data sets we used a model grid with a horizontal discretization of 2 km × 2 km beneath the station array. The central domain of 21 × 21 cells is padded by 15 planes in all four horizontal directions, where cell sizes increase laterally by a factor of 1.3. The vertical discretization is the same as for the forward model. All inversions were started from the prior model (see below), in all cases a homogeneous half-space.

3.2 Influence of prior model resistivity on phase tensor inversion

In ModEM, the 3-D MT inversion algorithm seeks to minimize the penalty function $\Psi = \Psi_d + \lambda\Psi_m$ consisting of a data regularization (data misfit) Ψ_d and a model regularization term Ψ_m weighted by the trade-off parameter λ (Egbert & Kelbert 2012). The model regularization is given by

$$\Psi_m = (\mathbf{m} - \mathbf{m}_{\text{prior}})^{\mathrm{T}}\, \mathbf{C}_m^{-1}(\mathbf{m} - \mathbf{m}_{\text{prior}}), \tag{5}$$

where $\mathbf{m}_{\text{prior}}$ is the prior model, $\mathbf{C}_m$ the model covariance, and $\boldsymbol{\lambda}$ a trade-off parameter. The model covariance $\mathbf{C}_m$ is a 3-D smoothing and scaling operator applied to the difference between the current model $\mathbf{m}$ and the *a priori* model $\mathbf{m}_{\text{prior}}$. Hence, the inversion tends to keep or return to the assumed prior resistivity, in particular where the model is poorly constrained. The model regularization scheme is very similar to that used in Siripunvaraporn & Egbert (2000), where specific mathematical detail are given in the Appendix. Implementation in ModEM is slightly different, but the concept is identical. Note that the model regularization scheme is similar to that of WSINV3DMT (Siripunvaraporn *et al.* 2005). Other regularization approaches are of course possible. In particular one could minimize

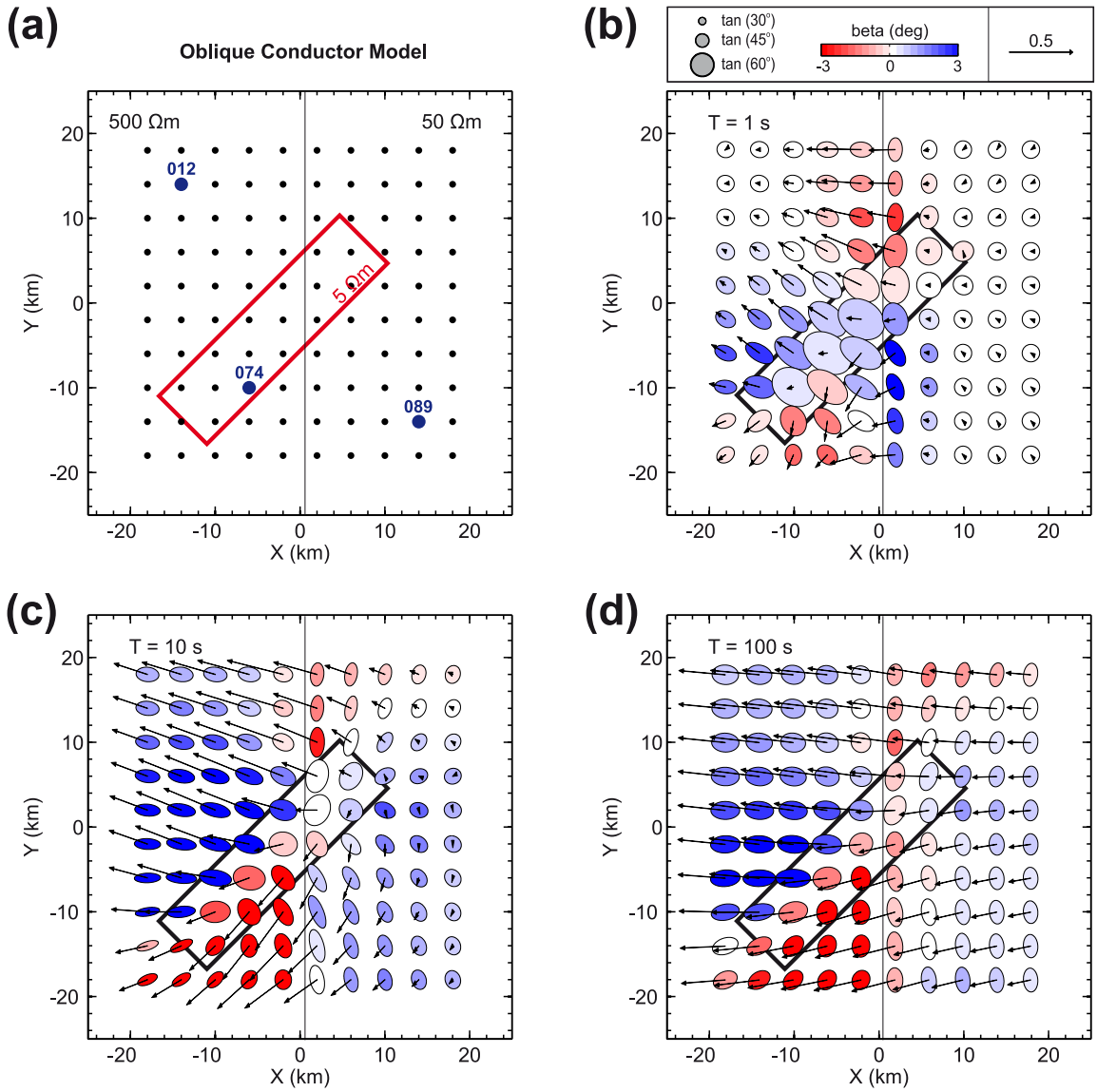

Figure 1. (a) The main structural feature of the synthetic model is a conductive 5 Ωm block of 30 km × 9 km × 9 km (length × width × height) located with its top at 2.56 km depth in the central model domain. The major axis of the conductive block is rotated 45° from the strike direction of the regional 2-D resistivity structure consisting of two half-layers of 500 and 50 Ωm between 0.1 and 75.0 km depth. The top (<0.1 km) and bottom (>75 km) layers are set to 100 Ωm. Black dots indicate site locations; blue dots mark locations of sites 012, 074 and 089. (b–d) Plot of phase tensors (fill = phase tensor beta value) and induction arrows (real part, Wiese convention) at periods of 1, 10 and 100 s. At periods >1 s, many sites of the Oblique Conductor data set show 3-D behaviour indicated by PT beta-values deviating significantly from zero (blue and red colours) and the rapid change of induction arrow directions across the conductive block.

the norm of first or second model derivatives without reference to any prior (e.g. Aster *et al.* 2011; Rodi & Mackie 2012). This would certainly affect inversion results, but would not have a first order effect on resolution. However, the regularization approach does have to be taken into account in interpreting the synthetic inversion tests in terms of resolving power of specific data types.

Phase tensor data contain little information about absolute values of subsurface resistivity, but rather are primarily sensitive to variations of the resistivity structure, similar to VTFs. Hence, we can anticipate that imposing a prior model, as ModEM does, will have a substantial effect on the subsurface image produced by the inversion. As in practice the correct background resistivity would be unknown, we started PT inversion of the undistorted OC data from a set of five homogeneous half-space models between 10 and 1000 Ωm. Data errors were set to 3 per cent of $|\Phi_{ij}|$ combined with a floor of 0.03. The corresponding final inversion models are displayed in Figs 2(a)–(e).

In all inversion results, the main structures and resistivity contrasts of the OC model are imaged in approximately the correct location. The obtained resistivities, particularly for the two half-layers, depend on the resistivity value of the prior model. But all inversions correctly reproduce the magnitude of the resistivity contrast between the two half-layers (10:1). The logarithmic average of the regional scale background structure given by the two half-layers is 158 Ωm. Hence using a prior model of 100 Ωm (Fig. 2c), the recovered half-layer resistivities are closest to that of the true model. For prior resistivities below the regional average of 158 Ωm, resistivities of the inverse models are underestimated (Figs 2a–c) and they are overestimated for prior model resistivities >158 Ωm (Figs 2d–e).

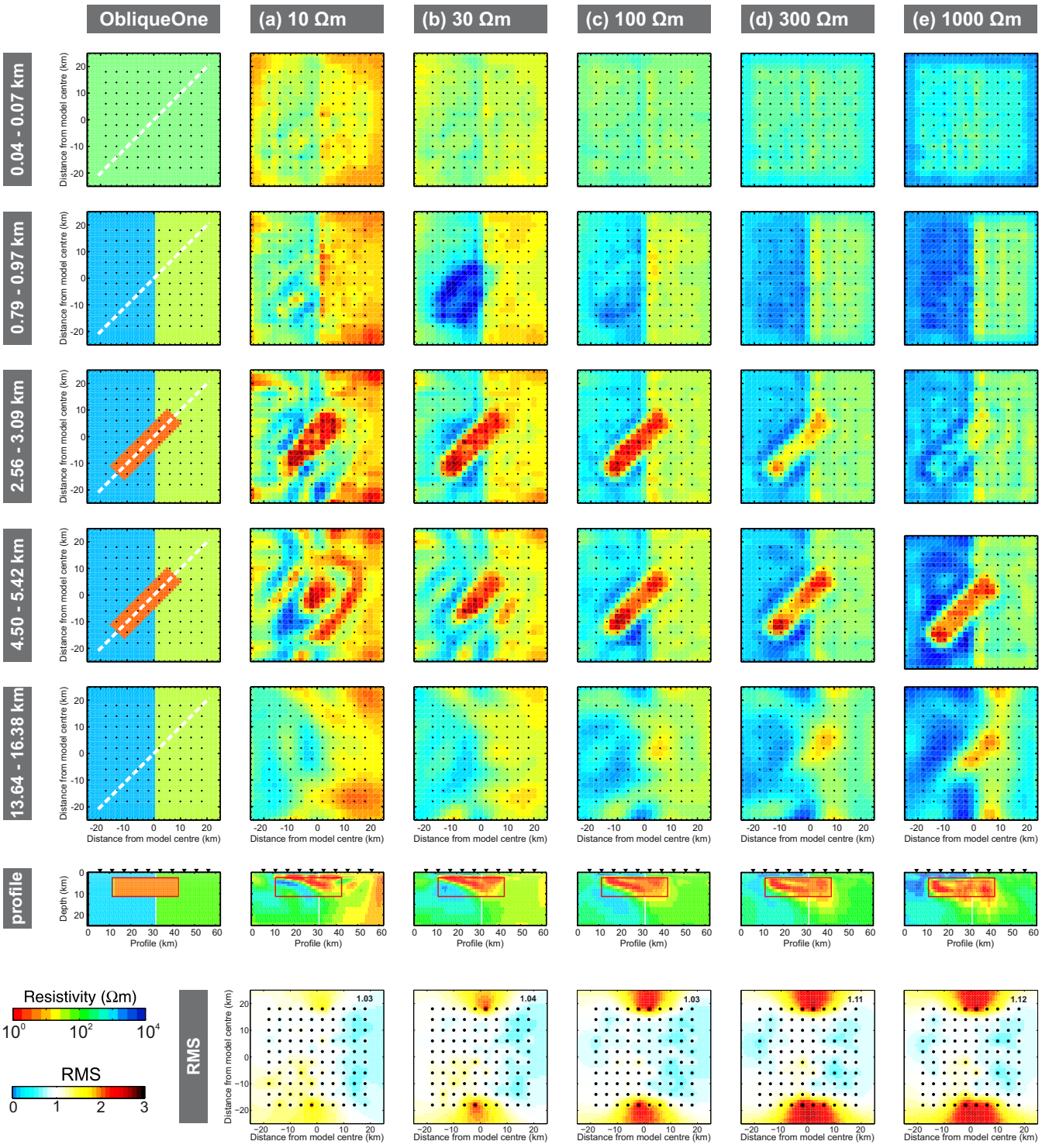

Figure 2. Resistivity models obtained from inversion of phase tensors (OC data set, *cf.* Fig. 1), displayed as horizontal slices at various depths and along a profile along the major axis of the oblique conductor (OC); the left-hand column displays the original OC model. Lowermost panels show final rms errors per site. (a)–(e) The dominant structures of the OC model are resolved by all inversion results. The resistivity level and, hence, depth location of the OC are biased by the resistivity of the prior model. Lateral conductivity variations, however, are similarly recovered in all results.

In contrast, the absolute resistivity of the conductive block is nearly independent of the prior model and always close to the true value of 5 Ωm for all inversion models. The lateral extent of the conductive block is similarly well constrained by the 3-D PT inversions, independently of the prior model (*cf.* profile slices in Figs 2a–e). The array of stations completely covers the conductive block and the boundaries of the conductive block are sampled densely. The upper and lower boundary of the conductive block show a stronger dependence on the prior model. When prior resistivities below the regional average (10–100 Ωm, Figs 2a–c) are used for PT inversion, the conductive block appears at shallower depth than in the true model. For prior model resistivities above the regional average

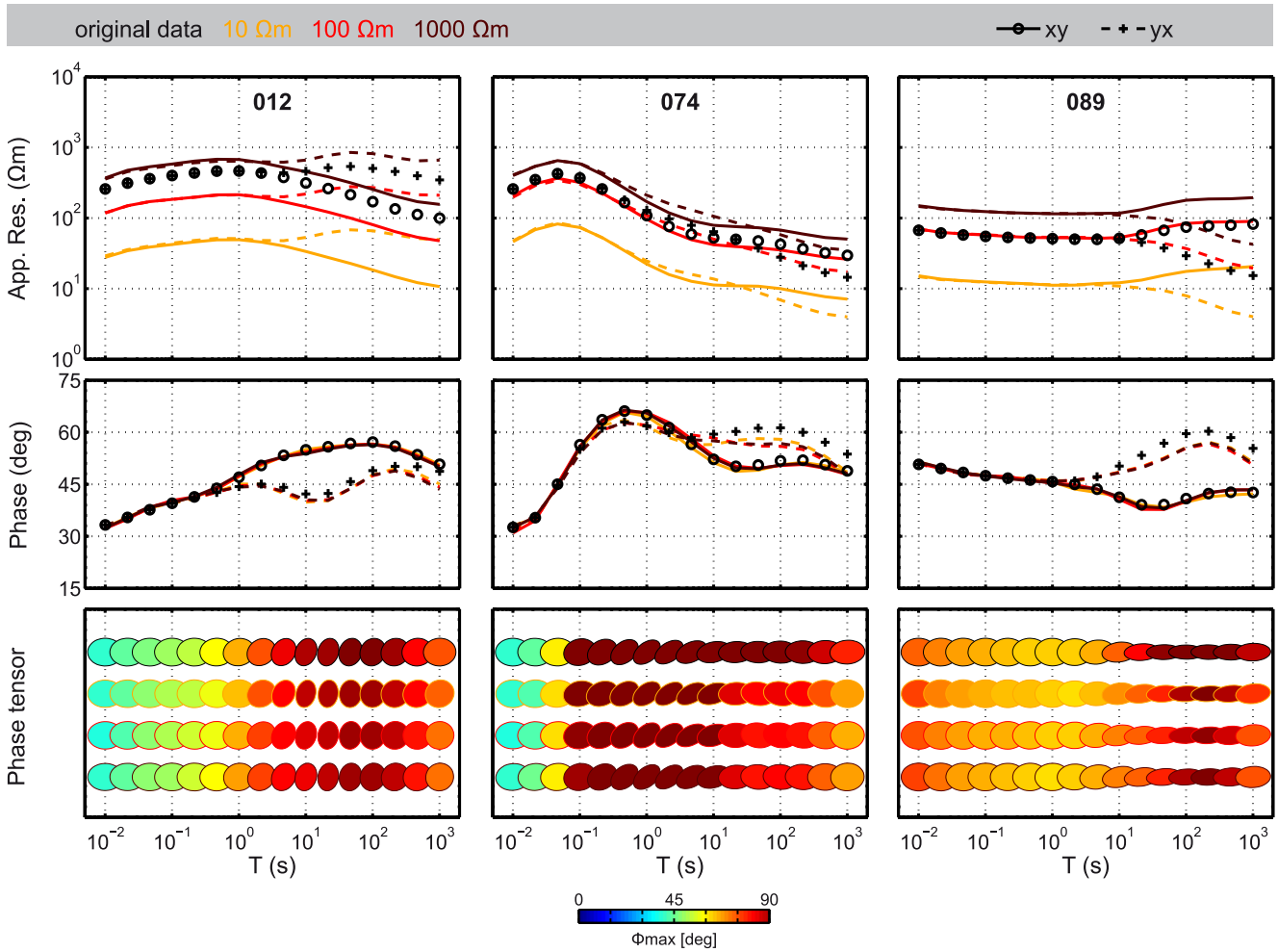

Figure 3. Comparison of 'observed' simulated data (symbols) and PT inversion model responses (lines) for three different prior models (10, 100 and 1000 Ωm) at selected sites (see Fig. 1 for site locations); impedance data for PT inversion results were obtained by forward modelling of the final resistivity model (*cf.* Figs 2a, c and e). Phase tensor data are displayed as normalized ellipses coloured with value of Φ*max*; top row is original data followed by inversion results for 10, 100 and 1000 Ωm). Using a 100 Ωm half-space as *a priori* model, PT inversion recovers absolute resistivities in the centre of the model (074, 089); towards the edges of the station array, the prior model resistivity plays a more important role (012). If the prior resistivity is below (above) the regional average (10 or 1000 Ωm) apparent resistivities (upper panels) are biased towards too low (high) values. However, phase curves and shape of apparent resistivity curves are recovered correctly.

(300 and 1000 Ωm, Figs 2d–e) the conductive block is moved to greater depth.

All inversions shown here converged to total rms values of <1.08 requiring 38–163 NLCG iterations. In addition, misfits are distributed smoothly across the array (lower panels in Figs 2a–e). The fewest NLCG iterations were required for prior model resistivities closest to the regional resistivity average, that is 300 and 100 Ωm.

For comparison, we also calculated impedance responses for the final PT inversion models obtained for prior model resistivities of 10, 100 and 1000 Ωm. The corresponding apparent resistivity and phase curves are displayed together with the original data in Fig. 3. Best data fit is achieved for a prior model with 100 Ωm background: PT inversion recovers both apparent resistivities (amplitude) and phase of the observed impedance data well (red lines in Fig. 3). As expected, using a prior model of 10 or 1000 Ωm, recovery of the impedance amplitude with PT inversion is poorer (orange and dark red lines in Fig. 3). The apparent resistivity curves of the PT results range between 0.5 and 1 decades below (above) the true OC data. However, the shape of the apparent resistivity curves and the phases are matched by all inversion results indicating that the structure of the resistivity distribution was recovered successfully.

Overall, the observed dependence on the prior model resistivities is consistent with the results obtained by Patro *et al.* (2013) for inversion of PT data with WSINV3DMT. In their study, the authors found that amplitudes of resistivity contrasts are imaged well independently of the prior model, whereas recovered absolute resistivity values were biased towards the prior model resistivity values. Consequently, for a synthetic test model, depth location and thickness of an isolated block was under- or overestimated if prior resistivities are below or above the regional resistivity, respectively.

Moreover, the outcome of our test and the study of Patro *et al.* (2013) is comparable to the results for inversion of VTFs for different prior models (Siripunvaraporn & Egbert 2009). Similar to PT data, VTFs only confer information about relative conductivity variations in the subsurface but do not contain absolute resistivity levels. For a synthetic example, Siripunvaraporn & Egbert (2009) describe similar dependencies on prior model resistivities for VTF inversion with respect to scaling of absolute resistivities, depth location of bodies, and final overall misfits. Sensitivities to horizontal

and vertical conductivity variations differ, however, for PT and VTF data (Booker 2013).

3.3 Joint inversion of phase tensor and vertical magnetic transfer functions

In MT, transfer functions between horizontal and vertical magnetic field components (VTF) are commonly interpreted jointly with the impedance data. As VTFs are independent of electric fields, they are also free of galvanic distortion. Therefore, we tested joint inversion of phase tensor and VTF data for the OC data set; data errors for PT data were the same as for previous examples, for the VTF data we used constant errors of 0.02. As before, we used homogeneous half-spaces of five different resistivities between 10 and 1000 Ωm for the prior models; the corresponding inversion results are summarized in Fig. 4.

When inverting phase tensor data jointly with VTF data, the influence of the starting model on the inversion outcome lessens (Figs 4a–e) compared to PT-only inversion (*cf.* Fig. 2). In particular, for starting model resistivities below the regional average (10–100 Ωm, Figs 4a–c), integration of VTF data improves recovery of the high resistivities of the background half-layers (*cf.* Figs 2a–c). In addition, the image of the conductive block in the central part of the model appears more focused.

Since VTF data—as PT data—sense only relative conductivity changes this result may appear surprising at first. However, both data types are associated with different sensitivity patterns: the spatial distribution of electric current density that determines VTF does not have a one-to-one correspondence to the phase of the electric and magnetic fields that determine PT data (Booker 2013); compared to the phase tensor, VTF data are particularly sensitive to horizontal resistivity changes, but less sensitive to vertical conductivity gradients. Our results indicate that the combination of both data types can improve recovery of the true resistivity structure.

These improvements can also be recognized when examining the data fit in terms of apparent resistivities and phases (Fig. 5). For the joint inversion result, maximum deviation of apparent resistivities amplitudes is about 0.5 decade, a significant improvement when compared to PT-only inversion results (*cf.* Fig. 3). In particular at sites located in the left half of the array above the higher resistive 500 Ωm half-layer (site 012, left-hand panel in Fig. 5; see Fig. 1), combination of the two data types results in better recovery of the true resistivities and, consequently, true impedance amplitudes. We suppose that the contribution of VTF data is larger for sites on the left-hand side as the horizontal conductivity contrasts, which are located in the centre of the model, affect more sites on this side (skin effect). Towards the right-hand side of the contrast, induction arrow amplitudes are decaying faster (Fig. 1b–d) and data become small compared to their error bounds.

Despite these improvements, inverse models of PT + VTF data are still recognizably influenced by the prior model. As previously mentioned, the ModEM inversion penalizes smoothed deviations from a prior model and prefers solutions close to the prior model (*cf.* eq. 5). Hence, inversion of any data type including impedances or apparent resistivities which carry amplitude information will also tend to be biased toward the prior model. For comparison, we inverted the undistorted impedance data of the OC model for a series of different starting model resistivities. The results for homogeneous half-spaces of 10, 100 and 1000 Ωm are summarized in Figs 6(a)–(c); data errors were set to 3 per cent of $|Z_{ij}|$ in combination with a floor of 3 per cent of $|Zxy^{*}Zyx|^{1/2}$ for the diagonal elements. The final models show that resistivities of the regional scale structures are underestimated for starting model resistivities below the regional average (10 Ωm, Fig. 6a) and overestimated if starting from a more resistive initial guess (1000 Ωm, Fig. 6c). For too high starting resistivities (1000 Ωm, Fig. 6c), the depth location of the conductive block is biased towards greater depth. However, the influence of the prior model is weaker than for PT or joint PT + VTF inversion (*cf.* Figs 2 and 4).

All inversions discussed above converged to the target rms requiring different number of NLCG iterations; in general, fewest NLCG iterations were required for starting model resistivities closest to the regional resistivity average, that is 300 and 100 Ωm (Fig. 7).

3.4 Inversion of the distorted data set

To illustrate the influence of galvanic distortion on impedance inversion and to test the PT inversion scheme, we also generated a randomly galvanically distorted data set by multiplying the undistorted impedances with a (real) distortion matrix **C**

$$\mathbf{Z}' = \mathbf{CZ}. \quad \mathbf{C} = \begin{pmatrix} c_{xx} & c_{xy} \\ c_{yx} & c_{yy} \end{pmatrix}. \tag{6}$$

The distortion parameters c_{ij} were taken from normal distributions with mean values of 1 (c_{xx} and c_{yy}) and 0 (c_{xy} and c_{yx}) and standard deviations of 1/3, that is the distortion parameters are distributed around their unity (matrix) values (Fig. 8a). We tested a range of values for the standard deviation and adjusted its value so that the resulting set of impedances appeared as obviously distorted both in amplitude and phase, but we ensured that changes in apparent resistivity amplitudes would be below 1.5 decades. For more severely affected data, we expect that distortion is obvious and distorted impedances are excluded from inversion. In Fig. 8(b) we illustrate the effect by applying all 100 sets of C to the data of one particular site. To test the effect on 3-D inversion, the distortion parameters were randomly distributed over all sites of the array. Prior to inversion, 3 per cent Gaussian noise was added to the distorted impedance tensor elements. The phase tensor data were derived from these distorted and noisy impedance data. Comparison of the distorted and the previously used undistorted data set shows that the distortion applied to the impedances causes a slight bias in phase tensor invariants Φmax, Φmin and β (Fig. 8c).

We invert both impedance and PT data. Based on the results above (Figs 2, 6a–c), we chose a homogeneous 100 Ωm half-space as starting and prior model resistivity for the inversions; all inversion parameters and data settings were the same as before.

Inverting distorted impedance data, results in a deep-reaching distortion of the model structures (Fig. 6d). A very rough and incoherent pattern of resistivities can be observed in the upper layers, which can be interpreted as an attempt of the inversion to account for static shift within the model domain. The spatial extent of these artificial surficial anomalies is larger than the inductive scale length and therefore alters the dimensionality of the responses: cross-plots of phase tensor parameters Φmax, Φmin and β scatter (lower panel in Figs 6d) and misfit is significantly higher than for inversion of undistorted impedances or phase tensor data (lower panels in Figs 6a–c, e). As a consequence, the image of the regional scale structure is distorted. In the example, the top of the oblique conductor and the surrounding background structure at 2.5 km depth, which is clearly resolved under normal circumstances, appears blurred. Only the very deep structure below 5 km depth is recovered with similar quality as for undistorted data (*cf.* Fig. 6b).

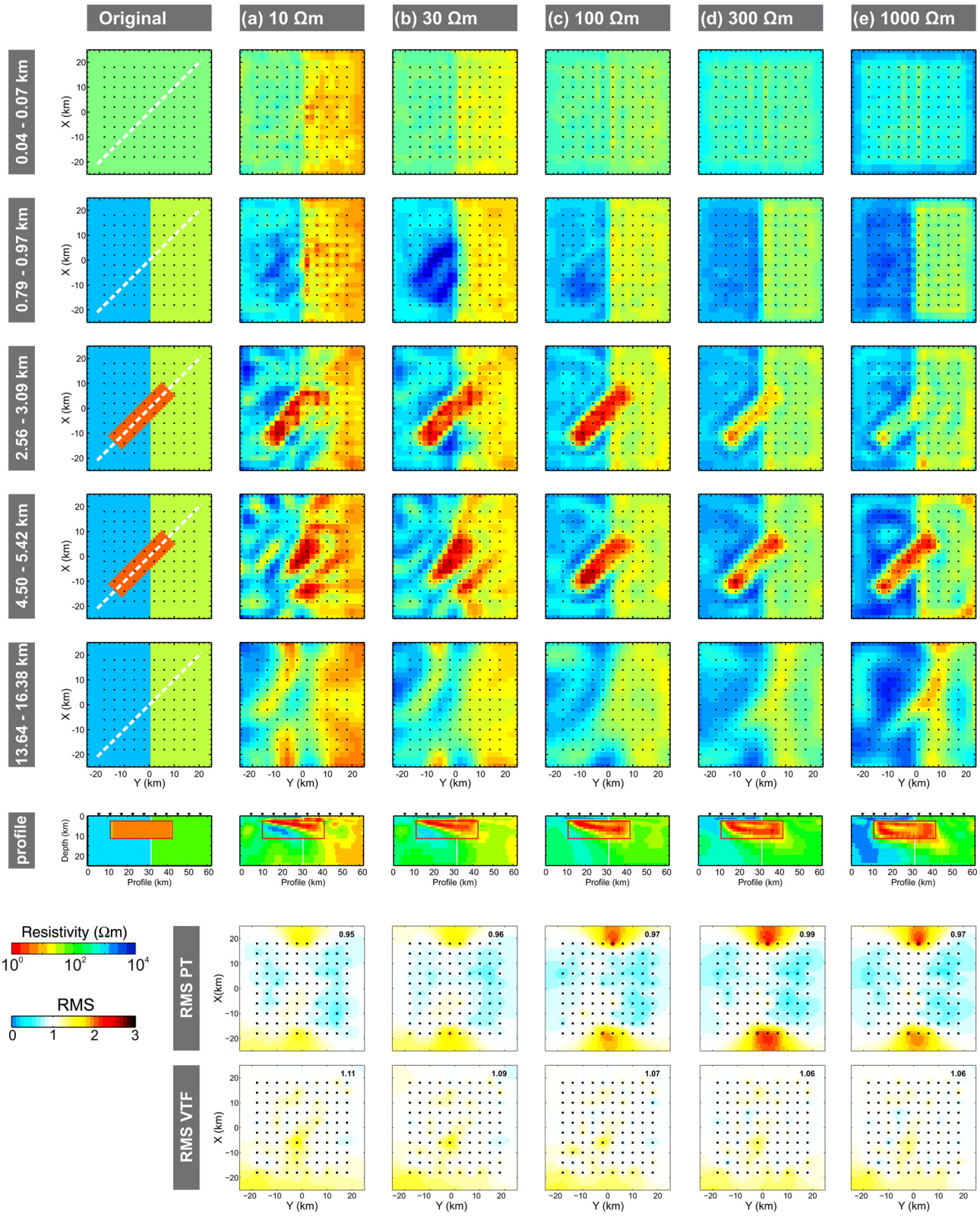

Figure 4. Resistivity models obtained from joint inversion of phase tensors and VTFs (OC data, *cf.* Fig. 1), displayed as horizontal slices at various depth and along a profile along the major axis of the oblique conductor (OC); the left-hand column shows the original OC model. (a)–(e) The dominant structures of the OC model are resolved by all inversion results. The resistivity structure of the inversion models is closer to the true OC model than the PT-only results, in particular if the *a priori* resistivity is below the regional average of 158 Ωm (a–c; *cf.* Fig. 2).

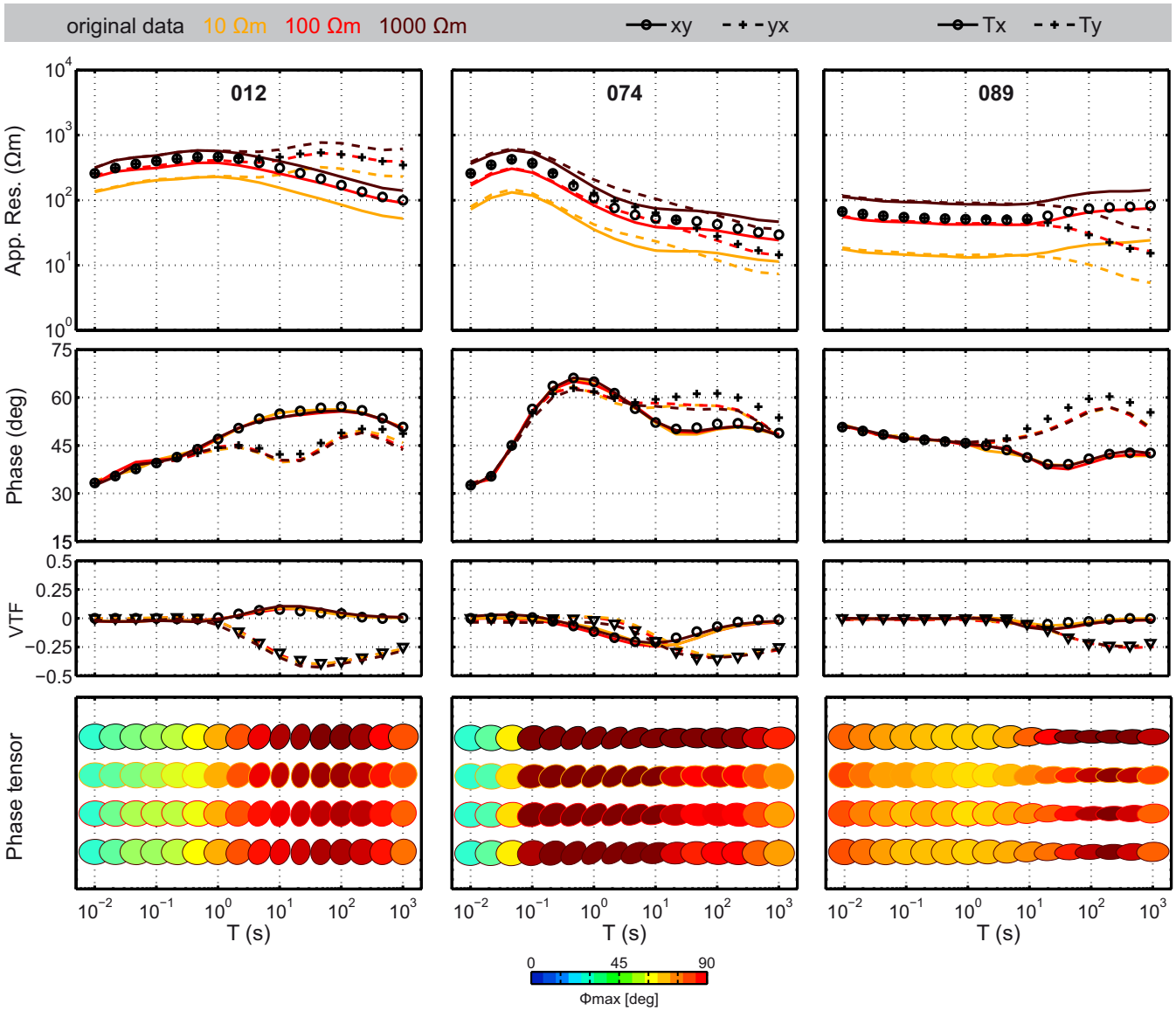

Figure 5. Comparison of 'observed' data (symbols) and PT + VTF inversion model responses (lines) for three different prior models (10, 100 and 1000 Ωm) at selected sites (see Fig. 1 for site locations); impedance data for joint PT + VTF inversion results were obtained by forward modelling of the final resistivity model (*cf.* Figs 4a, c and e). Phase tensor data are displayed as normalized ellipses coloured with value of Φ*max*; top row is original data followed by inversion results for 10, 100 and 1000 Ωm). If the prior resistivity is off the regional average (10, 1000 Ωm), joint inversion of PT + VTF data improves recovery of absolute resistivity values compared to PT-only inversion (Fig. 3): apparent resistivity amplitudes are closer to the original data.

Furthermore, inversion of distorted Oblique Conductor impedance data requires three to five times more NLCG iterations for convergence than for undistorted impedances and terminates with significantly higher overall rms values (3.09 for 100 Ωm starting model).

In general, the spatial extent of surface artefacts is related to the inversion setup, including mesh discretization with respect to site distances, minimum periods, background resistivity, and setting of smoothing (regularisation) parameters. The finer the discretization and the less the smoothing, the smaller the artefacts can be. In our example the horizontal discretization (2 km) in the central part of the inversion model mesh is relatively large with respect to the site spacing (4 km), and skin depth of the shortest periods (∼0.5 km). Near-surface artefacts inserted to compensate for the applied distortion are inevitably large enough to respond also inductively, and to influence data from neighbouring sites. This explains the relatively high rms value achieved, and the contamination of the image of the OC. The spatial extent of the anomalous structures reduces if the horizontal discretization is refined (e.g. to 1 × 1 km^2); however, notable effects are still observed until several km depth extending beyond the upper boundary of the conductive block. In the very large-scale 3-D inversion example presented in Meqbel *et al.* (2014) relative magnitudes of discretization (12.5 km) inter-site spacing (70 km), and minimum skin depth (∼15 km) are more favourable for direct 3-D modelling of galvanic distortion. In practice, mesh discretization and smoothing must be chosen as a trade-off between desired (fine) model grid and limitations of computer memory and/or run-times. Keeping discretization sufficiently fine may be especially difficult for the common situation where sites are not on a relatively uniformly grid (as in the study of Meqbel *et al.* 2014), but rather are collected along a series of denser profiles, with relatively wider profile spacing.

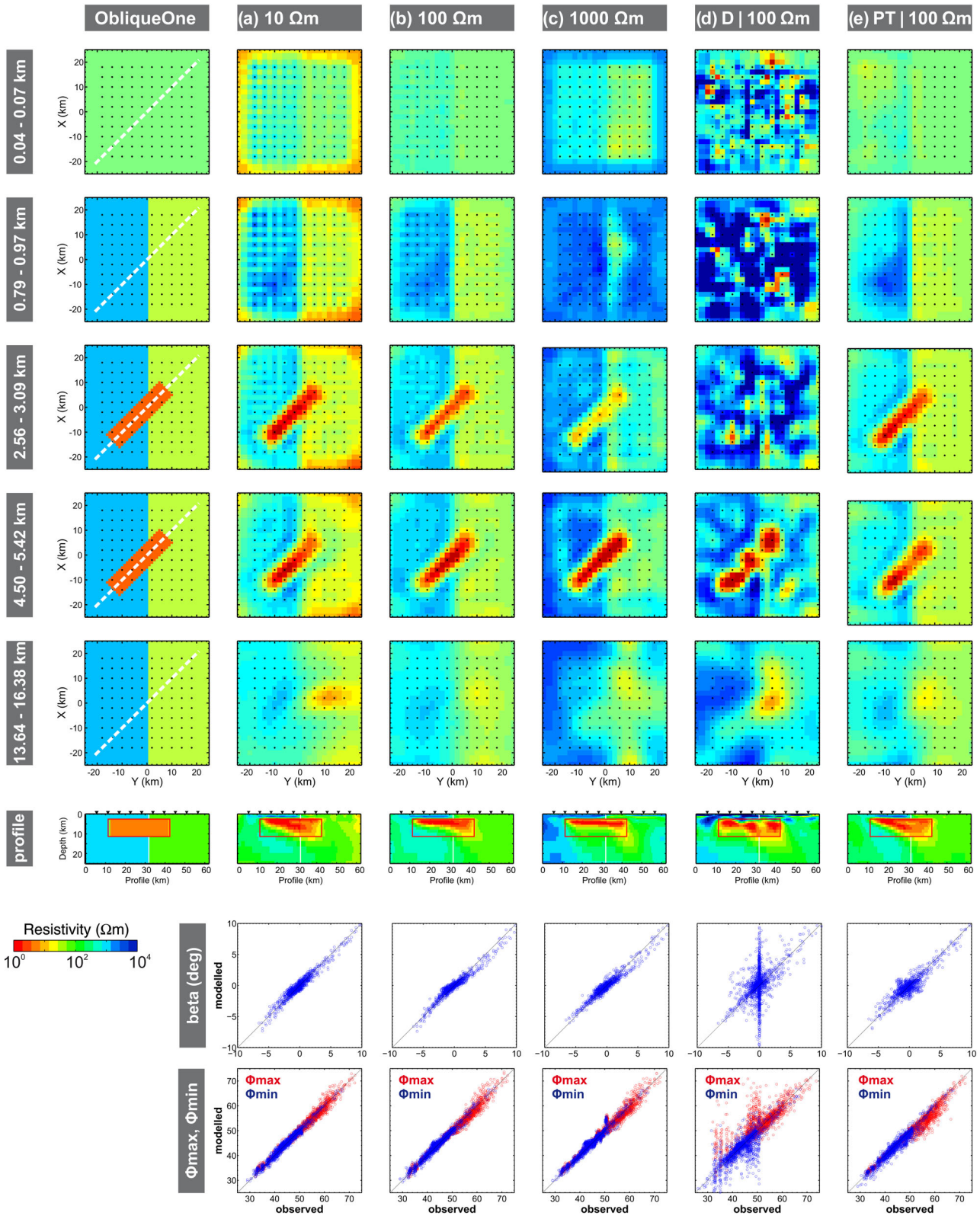

Figure 6. 3-D resistivity models obtained from inversion of the OC data set; left-hand column shows the original OC model. (a)–(c) Inversion results obtained using impedance data for different prior model resistivities. (d)–(e) Inversion results of synthetically distorted OC data (static shift) obtained using impedances (d) and phase tensor data (e). Final rms for inversion of distorted impedances in (d) is 3.09; all other inversions converged to the target rms of 1.03. Bottom panels: Crossplot of phase tensor parameters beta, Φ*max*, and Φ*min* for inversion responses (modelled) versus inverted (observed) data.

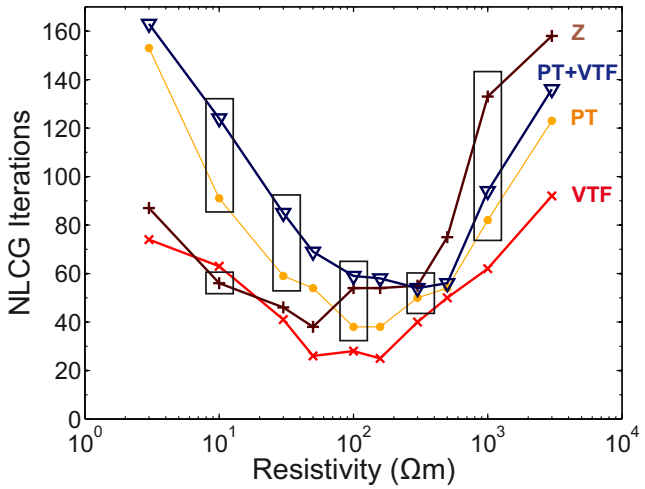

Figure 7. Total number of NLCG iterations required until convergence plotted versus *a priori*/starting model resistivity for inversion of different data types of the undistorted OC data set; PT Phase tensor, VTF vertical magnetic transfer functions, Z impedances; boxes indicate results for which resistivity models are shown in Figs 2 (PT), 4 (PT + VTF) and 6 (Z). For all data types, the number of NLCG iterations depends on the prior model resistivity; the lowest number was required for prior models with background resistivities between 100 and 300 Ωm, that is close to the regional resistivity average of 158 Ωm.

Contrary to the impedance data, inversion of the phase tensor (Fig. 6e) data recovers the OC resistivity structure with similar quality as for the undistorted data set (*cf.* Fig. 2c). Minor differences between the inversion models result from the differences in the synthetic noise of the respective impedance and consequently the phase tensors between the two data sets (*cf.* Fig. 8c). Comparison of Figs 6(e) and (d) illustrates clearly the value of phase tensor inversion in presence of galvanic distortion.

4 FIELD EXAMPLE

4.1 Data set

The field MT data were collected at the San Andreas Fault between Parkfield and Cholame, central California, USA (Fig. 9), where the fault's mechanical state changes from creeping to being locked, and where a source area of non-volcanic tremors has been located (e.g. Nadeau & Dolenc 2005; Shelly *et al.* 2009; Zhang *et al.* 2010). Between 2005 and 2008, the Geo-Electromagnetics group of GFZ Potsdam deployed more than 250 MT sites along seven parallel profiles across the fault system, covering an area of 130 km × 60 km across and along strike, respectively. The profile separation is roughly 10 km, site spacing along the profiles varies from 0.5 km in the central parts across the SAF to approximately 10 km towards the profile ends.

MT transfer functions were obtained for periods between 0.01 and 20 000 s using robust single site and remote reference processing routines (Egbert & Booker 1986; Egbert 1997; Ritter *et al.* 1998; Weckmann *et al.* 2005). The quality of the transfer functions is generally high for the entire array and all periods. A detailed description of the data processing procedure is given in Becken *et al.* (2008, 2011).

The data set exhibits a predominant geo-electric strike direction of N41°W (Becken *et al.* 2011), which is consistent with the strike direction of the regional geology (Page *et al.* 1998). In a strike-aligned coordinate system, the fields (almost) decouple into TE- and TM-modes and information on large-scale subsurface structures is split up between the individual impedance components: The larger *Zyx* component contains information on high resistivities of the Pacific plate while the smaller *Zxy* component contains the information on a high-conductivity zone at depth. Phase tensor major axes show consistent alignments at long periods indicating quasi-2-D structures (Figs 10c–d). However, phase tensor beta values exceed ±1° at 50 per cent and ±3° at 25 per cent of the data points, which indicates a significant influence of 3-D subsurface structures on the data (*cf.* Caldwell *et al.* 2004). The influence of 3-D structures is most pronounced in the period range between 10 and 2000 s (Fig. 10; see also Tietze & Ritter 2013). A detailed discussion of prior MT inversion and modelling results as well as a geologic interpretation of the data set are given in Becken *et al.* (2008, 2011) and Tietze & Ritter (2013).

4.2 3-D inversion setup

We tested the new phase tensor inversion schemes with the Parkfield MT data set. In this paper we focus on inversion of the data set in terms of PT data and the influence of galvanic distortion on the 3-D inversion models. We used a subset of 73 sites of the Parkfield MT array data to achieve a more regular distribution of observations which is advantageous for recovery of the regional conductivity structure (see Tietze & Ritter 2013). For the 3-D inversion results shown in the following, we used 18 periods distributed evenly on a logarithmic scale in the range between 0.08 and 11 000 s. Site spacing is approximately 10 km (white circles in Fig. 9). Preference is given to sites with high data quality, covering a wide period range and/or where both impedances and VTFs are available. In preparation for 3-D inversion, the impedance tensor elements and VTFs were rotated to the regional geo-electric strike direction (N41°W, Becken *et al.* 2011). Tietze & Ritter (2013) found that such a rotation is essential to reliably recover the resistivity structure of the survey area at depths >10 km. Otherwise, regional scale conductive features may remain undiscovered.

The corresponding model grid consists of 50 × 70 × 57 cells in the two horizontal and the vertical directions, respectively. The inner part comprises a uniform mesh of 20 × 40 × 57 with an edge length of 4.0 km. On all four sides, the central domain is padded with 15 planes where cell sizes increase laterally by a factor of 1.3. The vertical thickness is 25 m for the first layer; subsequent layer thicknesses successively increase by a factor of 1.2. Prior model resistivities were set to 10 Ωm. For all field data inversions, a rough bathymetry of the Pacific Ocean was included as *a priori* information. A resistivity of 0.3 Ωm was assigned to the ocean cells, and this model domain was kept fixed at all times during the inversion. Prior and starting models were always identical.

We invert all data types (Z, VTF and PT) separately as well as VTFs jointly with both impedances (Z) and phase tensors (PT). Table 1 summarizes the data errors used for each data type; the corresponding inversion results are shown in Figs 11 and 12.

4.3 Inversion results

Considering the inversion results on a regional scale, the outcome of 3-D inversion is in general very similar for all data types (Figs 11a–f, 12a–h). The main features of the resistivity structure which occur in all inversion results can be summarized as follows: At depths <10 km, the 3-D resistivity structure is dominated by a conductive

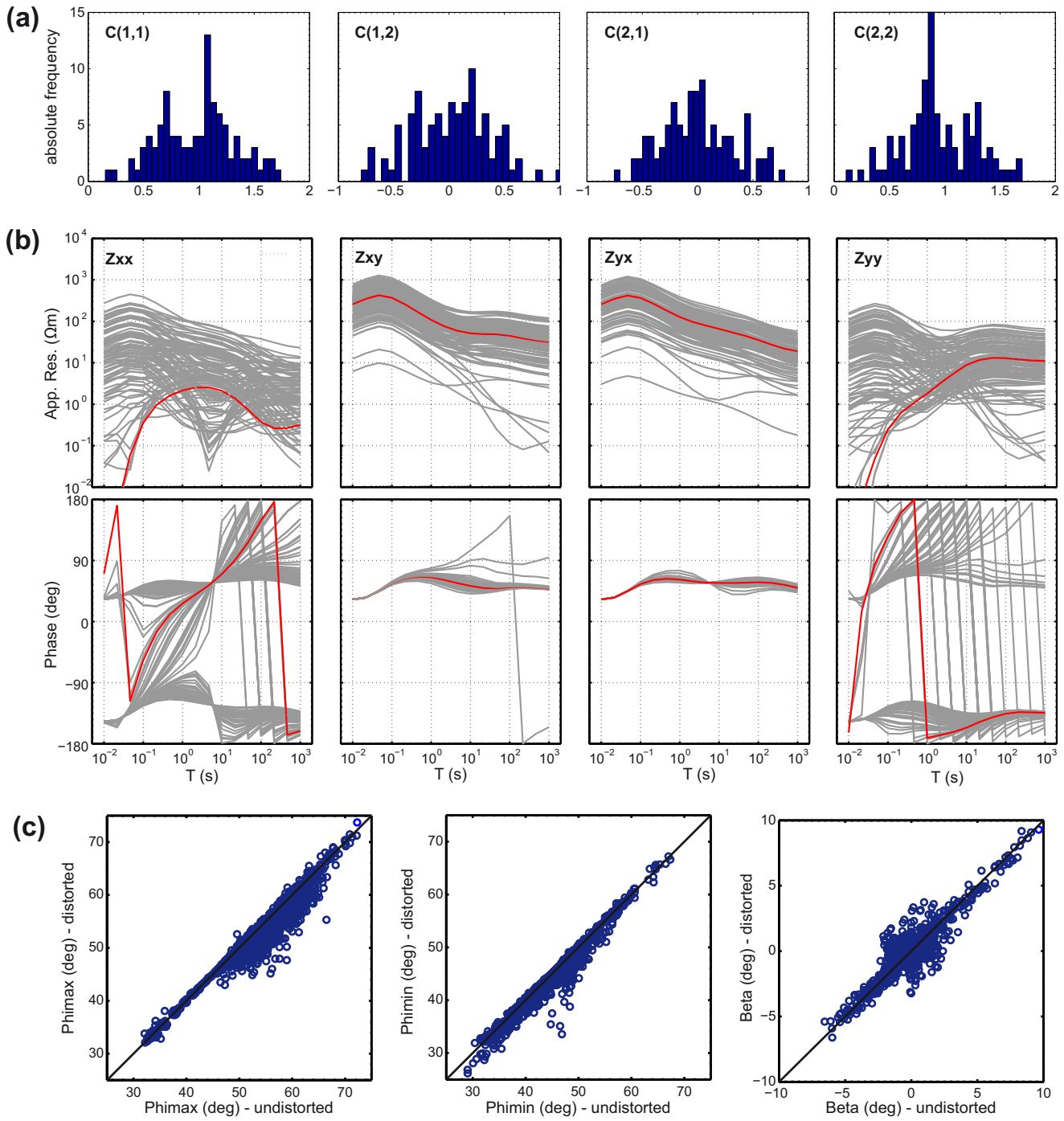

Figure 8. Synthetic distortion applied to OC data set. (a) Elements Cij of the distortion matrix **C** (*cf.* eq. 1a) are taken from a normal distribution with mean values of 1 (C11, C22) and 0 (C12, C21) and standard deviations of 1/3. 100 sets of distortion matrices C were generated from the randomly distributed Cij values. (b) The effect of the galvanic distortion values is shown exemplarily by applying the 100 sets of C to the responses of site 074 (*cf.* Fig. 1 for location). Red lines show original undistorted data; grey lines show the family of distorted data for each impedance component. (c) Crossplot of phase tensor parameters Φmax, Φmin, and beta for undistorted versus distorted data set.

(0.1–5 Ωm) sequences with thicknesses of approximately 2 km in most parts of the array but which reach 5–9 km in the San Joaquin valley. In areas close to the coast and along the surface traces of the San Andreas and Rinconada faults the conductive layer thins out and zones of high resistivities (200–1000 Ωm) reach close to surface. At mid-crustal levels (approximately 10–20 km), the models reveal resistive structures (200–5000 Ωm) extending from the coast to the SAF. A 10–20 km wide region west of the SAF appears as conductive (1–10 Ωm); this high-conductivity zone (HCZ) extends parallel to the SAF with its top located between 9 and 17 km depth. For a detailed discussion of the 3-D resistivity structure as well as previous 2-D interpretation of the data set refer to Tietze & Ritter (2013) and Becken *et al.* (2008, 2011).

PT inversion results of Figs 11(d) and (e) were obtained with different model covariance settings. For the model in Fig. 11(d), the same setup as for the impedance inversion was used, that is

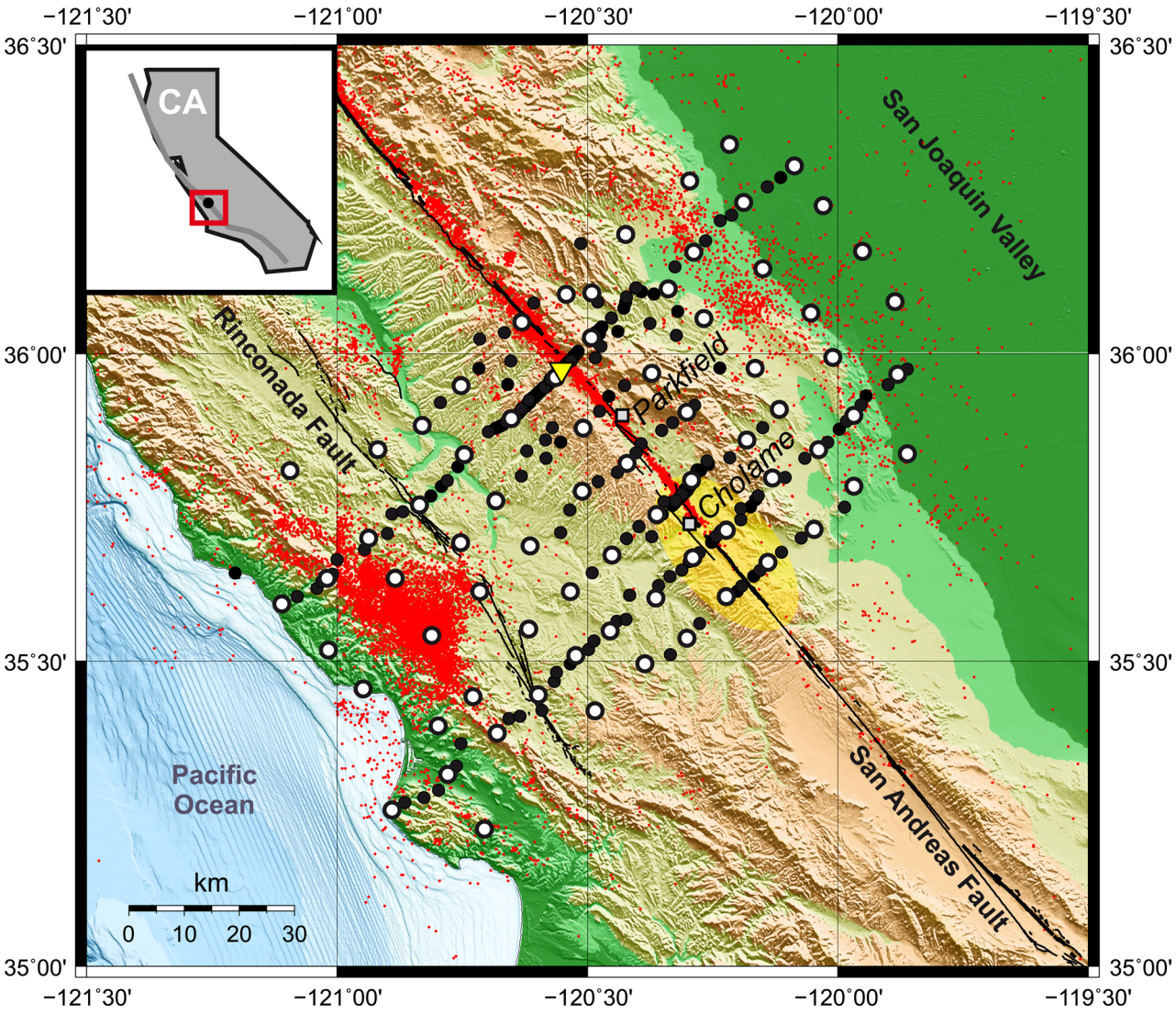

Figure 9. More than 250 MT sites were deployed along seven profiles across the San Andreas fault in the vicinity of Parkfield and Cholame in California, USA. The sites marked by circles cover an area of 130 km × 70 km. For 3-D inversion a subset comprising 73 sites (white circles) was used. The location of the San Andreas Fault Observatory at Depth (SAFOD) is indicated by a yellow triangle. Small red dots indicate seismicity (NCDEC 2002–2011, $m > 1.0$), the yellow shaded area outlines the main cluster of non-volcanic tremors after Zhang *et al.* (2010).

with enhanced smoothing along-strike. In contrast, for the result in Fig. 11(e), same scaling was applied for all three spatial directions (isotropic smoothing). Both inversions recover all of the major features of the subsurface, including the HCZ. The high resistivities of the Pacific Plate, however, are much better recovered if laterally isotropic smoothing is used (Fig. 11e). Other differences between the two models occur in the upper 10 km between the HCZ and the SAF as we observe a sequence of conductive structures with anisotropic smoothing. We consider this as an artefact as the structures vanish without deteriorating the data fit when using isotropic smoothing. Also, these spurious features are not present in the impedance and VTF-only inversion results.

In the following, we compare inversion results for different data types in more detail referring to PT and joint PT + VTF inversion results obtained with isotropic smoothing (Figs 11e–f). Fig. 12 shows slices along profiles 2 and 6 (see Fig. 9 for location) for inversion of the different data types. Main structures of the regional resistivity structure at depth >10 km are recovered similarly. Conductivities of the HCZ itself are similar for all inversion results.

Differences between the 3-D inversion results with respect to the regional structure manifest in the region surrounding the HCZ on the Pacific side of the SAF (labelled R in Figs 11 and 12). This is perhaps not surprising, as the high contrast between the conductive ocean and the highly resistive plate, right at the edge of the array, presents a very difficult challenge for 3-D inversion (see Tietze & Ritter 2013). In the impedance-only (Figs 11a, 12a and e) and the joint impedance + VTF (Figs 11c, 12b and f) inversion model, resistivities in region R exceed 500 Ωm, reaching values of up to 2000 Ωm. Previous studies of Tietze & Ritter (2013), Becken *et al.* (2011) and Wheelock (2012) showed that these high resistivities are essential to explain the data.

Inversion of PT data alone results in resistivities in the zones labelled with 'R' between 50 and 1000 Ωm (Figs 11d–e, 12c and g). These values are slightly below those obtained with the impedance inversion but are significantly above the prior model resistivity (10 Ωm). The resistive zones *R* are thus required structures, although amplitudes are not well constrained by PT data alone. However, inverting PT jointly with VTF data, resistivities in zone

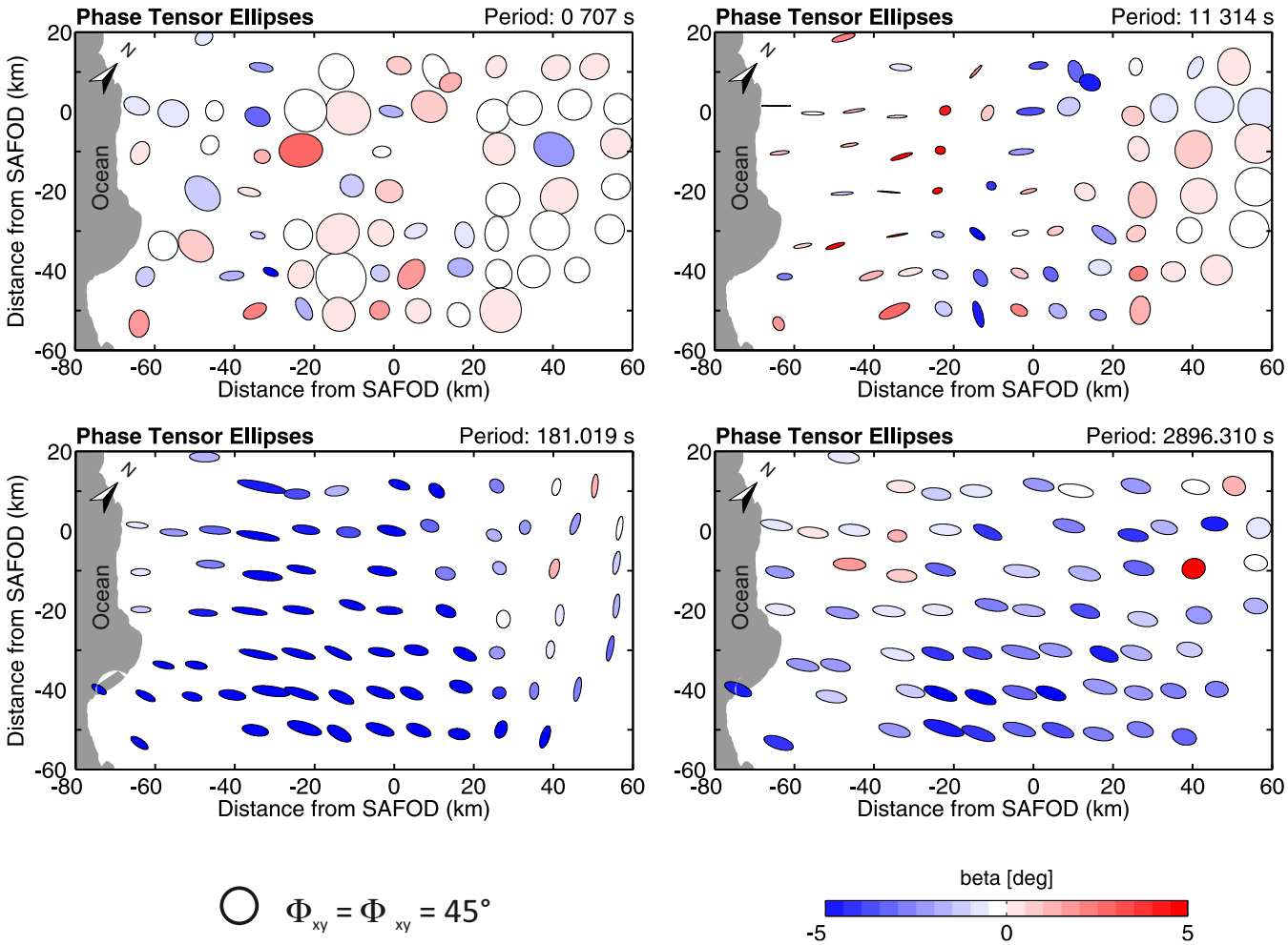

Figure 10. Phase Tensor ellipses for subset of the California data set and periods of 0.71, 11.3, 181 and 2896 s. Beta values significantly deviating from zero (red and blue colouring) indicate influences of a 3-D subsurface for periods >1 s. The orientation of phase tensor ellipses is consistent with a strike direction of N41°W.

Table 1. Data error settings for 3-D inversion of the Parkfield data set.

Data type (symbol)	Data errors
Impedance (Z)	3 per cent of $\|Zxy\|$ for Zxx and Zxy and 3 per cent of $\|Zyx\|$ for Zyx and Zyy floor of 5 per cent of $\|Zii\|$ for Zxx and Zyy
Phase tensor (PT)	3 per cent of $\|\Phi_{ij}\|$, floor 0.035
Vertical magnetic transfer function (VTF)	0.02

R range between 500 and 2000 Ωm (Figs 11f, 12d and h), nearly as high as the impedance results.

For the Parkfield region, the wide range of resistivities between approx. 0.1 and 10 000 Ωm is challenging in general when performing 3-D inversion, in particular for PT or VTF data which are more sensitive to the prior model. The chosen prior model background resistivities of 10 Ωm (for the central part of the model) appear to be a good match for the near-surface structures of this region. Together with the *a priori* information on the Pacific Ocean the initial guess for the shallow conductivity contrasts is probably close to the true situation and provides reasonable scaling at least for PT and PT + VTF inversions so that they do recover higher resistivities at depth.

Considering the VTF-only inversion result which reveals a relatively conductive deeper subsurface (Fig. 11b), the influence of the VTF on the joint PT + VTF inversion result seems surprising at first. Obviously, the different sensitivities of PT and VTF with respect to horizontal and vertical conductivity variations complement each other, at least for this data set from California. In particular, the significant influence of the high resistivities beneath the coastline and within the adjacent oceanic plate on VTF data in the coastal area contributes to the recovery of strong resistivity contrasts and extended zones of high resistivities in the joint inversion of PT and VTF data.

Moreover, the conductive features which appeared in the PT-only result of profile 2 (Fig. 12c) disappear when VTF data are added. Thus, we consider this structure an artefact caused by the poor recovery of high resistivities in the PT-only inversion result. With the inclusion of the additional small conductor, the 3-D inversion attempts to add a resistivity contrast between the conductive ocean and the high resistive Pacific Plate. Similar artefacts in the coastal area were observed in inversion results of VTF data (Fig. 11b) and inversion tests with synthetic data (Tietze & Ritter 2013).

Further to the SE beneath profile 6, the PT + VTF result (Fig. 12h) locates the HCZ at greater depth than the PT-only model, and is in better agreement with the impedance + VTF results (Figs 12f).

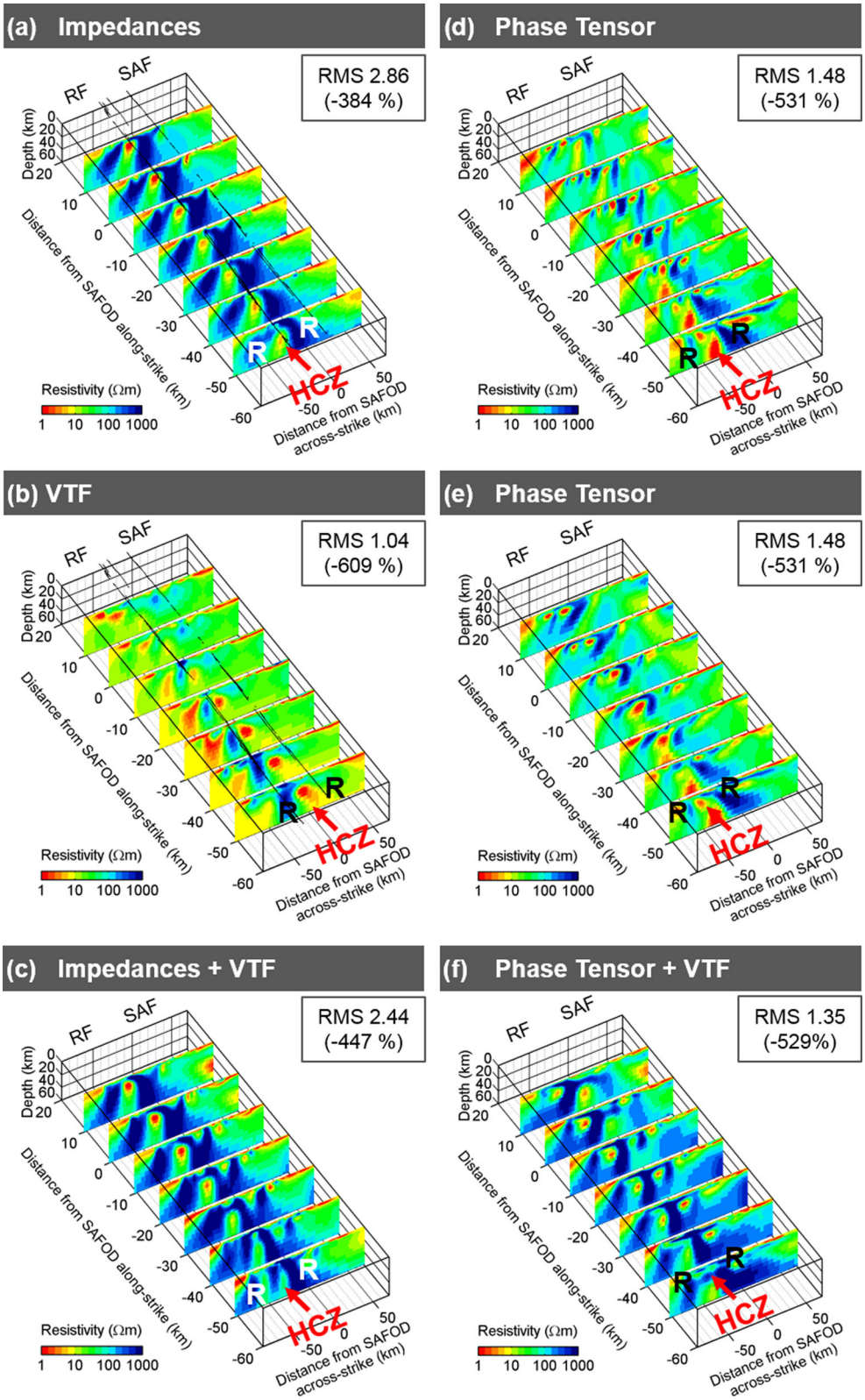

Figure 11. Resistivity models obtained for the Parkfield MT data set when inverting different data types (a)–(f); see text for 3-D inversion setup and Table 1 for error settings. Resistivity models are shown as profile slices along the seven profile lines (*cf*. Fig. 9). (a–d) smoothing enhanced parallel to strike; (e–f) isotropic model smoothing. Major feature of the deep, regional scale electrical conductivity structure is a strike-parallel highly conductive zone (HCZ) surrounded by areas of high resistivities (R).

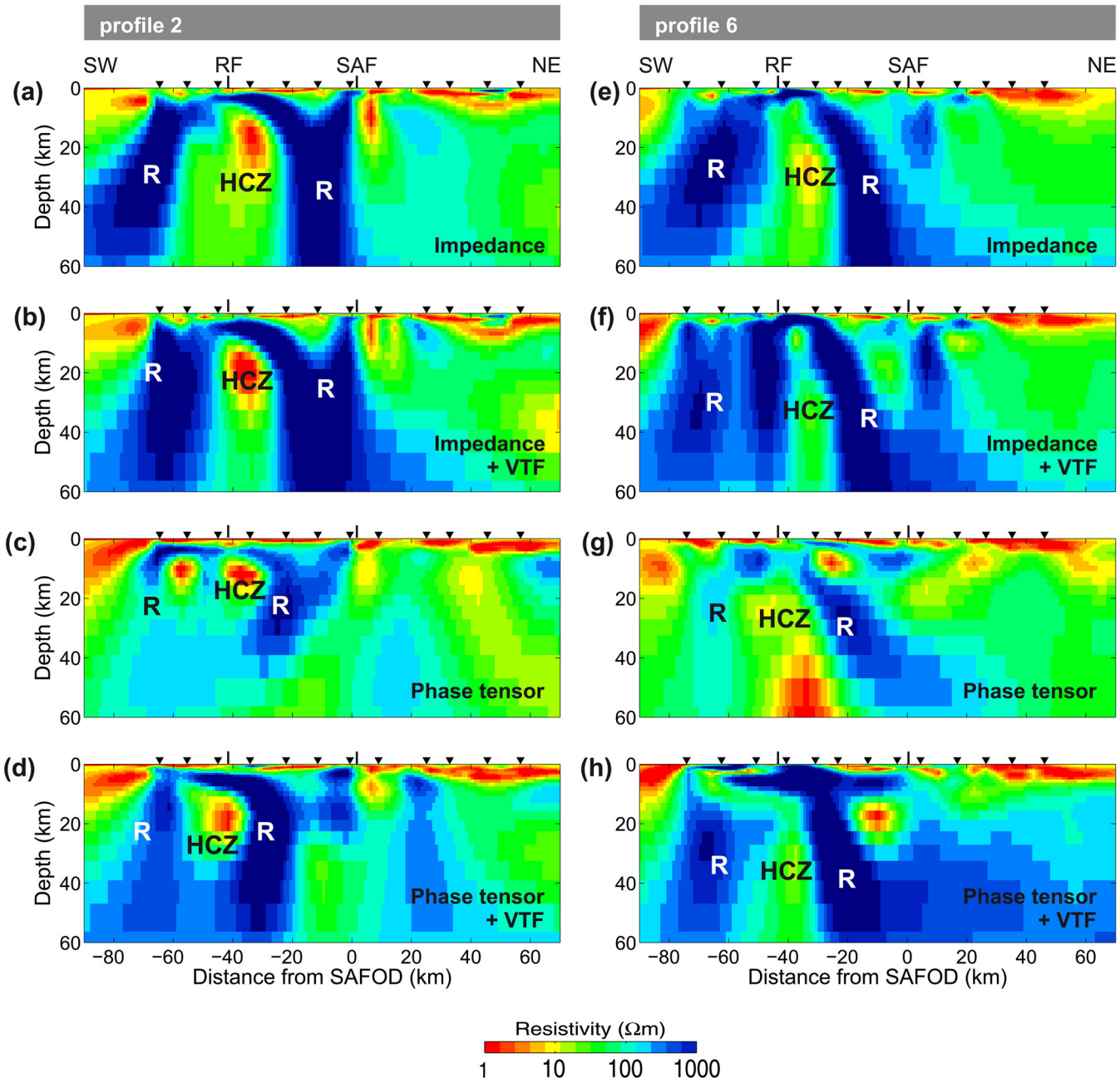

Figure 12. Profile sections along profiles 2 (a–d) and 6 (e–h) for inversion of the SAF data set (*cf.* map in Fig. 9) using different data types: (a) and (e) impedances, (b) and (f) impedances + VTF, (c) and (g) phase tensor, (d) and (h) phase tensor + VTF data. Corresponding inversion results along all seven profiles are shown in Figs 11(a), (c), (e) and (f). Major feature of the deep, regional scale electrical conductivity structure is a strike-parallel highly conductive zone (HCZ) surrounded by areas of high resistivities (R). Vertical lines mark surface traces of the Rinconada fault (RF) and the San Andreas fault (SAF).

In the synthetic examples of Section 3 similar differences in the depth location of the conductive block between PT-only and PT + VTF results occurred for inversions where the starting/prior model was more conductive than the average of the background resistivity structure (Figs 2a,b and 4a,b). Therefore, we interpret the inversion results for the PT data from California as a hint that the average resistivities should be significantly higher for the deeper parts of the survey region. Unfortunately, using higher prior model resistivities ($>10\,\Omega$m) leads to inversion results without a HCZ and consequently a significantly larger misfit, particularly at coastal stations. The HCZ is an essential model feature, which is easily missed if the model is oversmoothed and data not properly weighted (Tietze & Ritter 2013).

An areal impression of the near-surface structure of the entire survey area is given in Fig. 13 which shows horizontal slices through the 3-D inversion models of Figs 11(a), (e) and (f) at 0.25 and 1.45 km depth. In the uppermost 500 m, the impedance inversion model exhibits a highly variable, small-scale resistivity pattern which is much rougher than the resistivity distribution of the PT and PT + VTF results (upper panels in Figs 13a–c). The surficial features in Fig. 13(a) appear stretched along the SAF-parallel axis as a higher smoothing was enforced in this direction. At depths >1 km, the

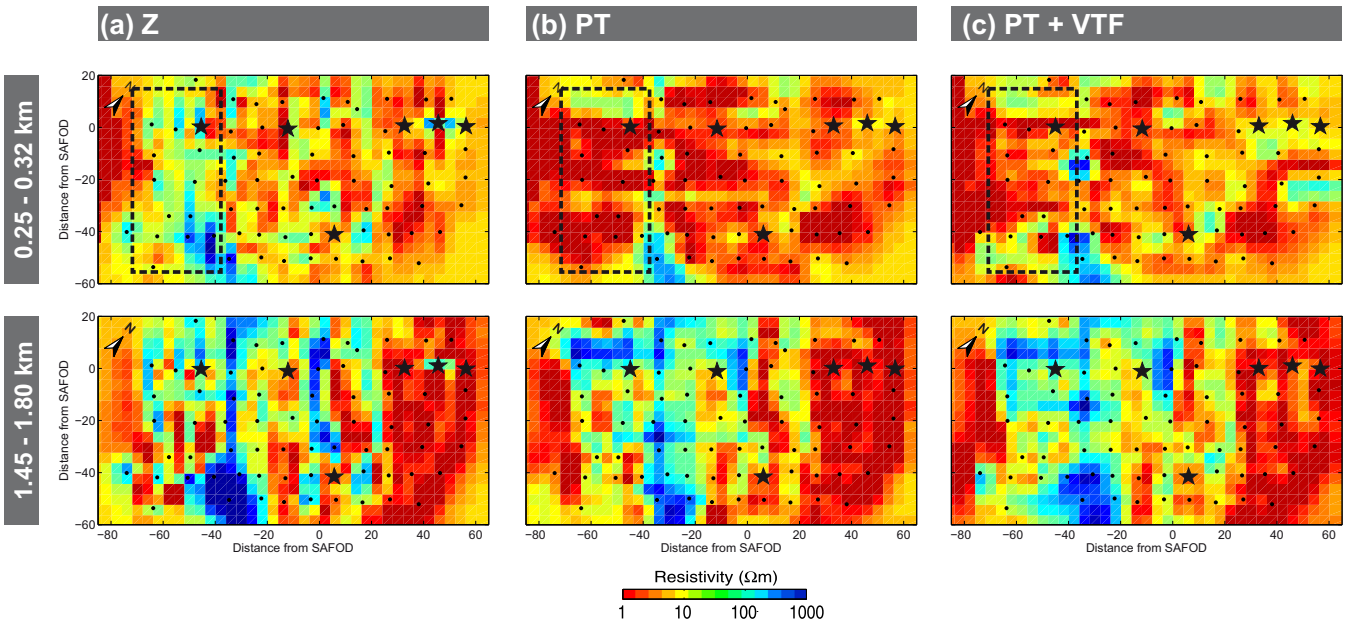

Figure 13. Near-surface structure of 3-D resistivity models obtained for the Parkfield MT data set shown in Figs 11 (a), (e) and (f); see text for inversion setup and Table 1 for data error settings. Asterisks indicate sites displayed in Figs 14 and 15 (from left to right: 403, 209, 509, 407, 408 and 409). Black dashed outline indicates regions where we suspect that near-surface structure of the PT-only inversion results is biased towards too low resistivities (see text).

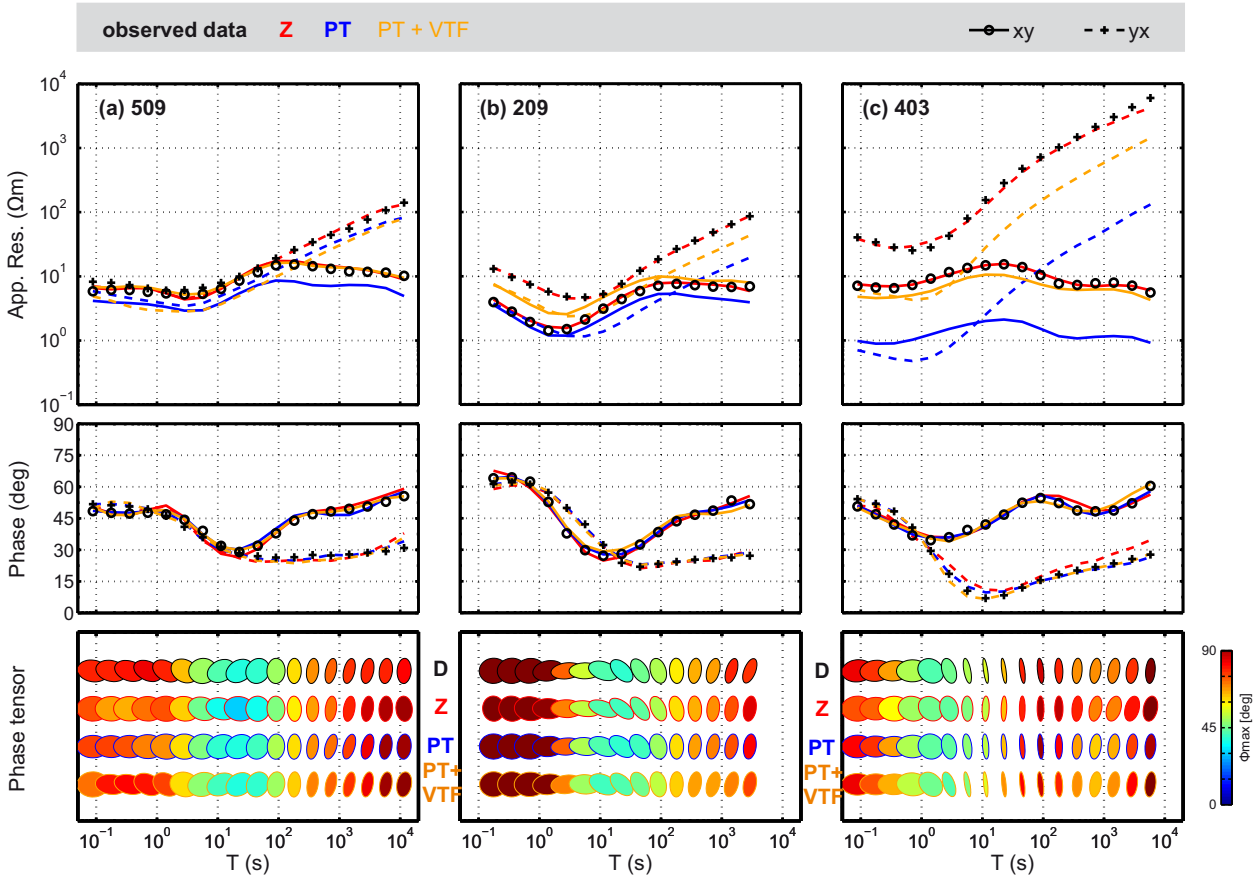

Figure 14. Data fit of resistivity models obtained with inversion of impedances (Z, *cf.* Fig. 11a) phase tensors (PT, *cf.* Fig. 11e), and joint inversion of phase tensor and VTF data (*cf.* Fig. 11f) at selected stations; see Fig. 13 for site locations. Apparent resistivity and phase data for PT and PT + VTF inversion results were obtained from forward calculation. Phase tensor data are displayed as normalized ellipses coloured with value of Φmax.

resistivity structures of all three results are much more similar and have comparable degree of roughness (lower panels in Figs 13a–c). These results agree with our impression, that the California MT array is largely unaffected by galvanic distortion. At short periods (0.1–10 s), off-diagonal apparent resistivities usually differ by less than half a decade between components and from site to site. In addition, diagonal elements are usually small at short periods but amplitudes increase towards longer periods (Fig. 14).

Consequently, at sites where distortion is small or non-existent, data fits of impedance and PT or PT + VTF inversion are comparable (Figs 14a,b and 15a,c). The results at site 209 (Fig. 14b) also show that impedance inversion models reproduce the data including distortion. For PT and PT + VTF inversions, off-diagonal apparent resistivity curves have a small offset from the observed data at periods <1 s. Modelled amplitudes of both apparent resistivity components are identical at short periods and do not reproduce the obvious distortion of site 209, which is different from the impedance inversion results. However, fit of impedance phases is comparable for all data types. When comparing the near-surface structure of the corresponding inversion models, we find small isolated resistors beneath site 209 in the impedance inversion results (Fig. 13a), which we consider artefacts as they are introduced to compensate for galvanic distortion. They are not present or only weakly expressed in the PT and PT + VTF models (Figs 13b and c). These results suggest that 3-D impedance inversion can compensate for (small amounts of) galvanic distortion of the Parkfield data set by introducing relatively small-scale artefacts mainly in the upper ∼15 layers (0–1.2 km) of the model. Comparison between inversion models obtained from distortion-free PT and VTF data can help identifying such artificial structures in general.

At some stations in the vicinity of the coast, PT-only inversion yields very low apparent resistivity amplitudes (Fig. 14c). Inversion models obtained from inversion of PT, and to some extent also PT + VTF, suggest extremely low resistivities (<1 Ωm) near the coast in the upper 500 m, whereas impedance inversion models suggest values of 10–50 Ωm (dashed outline in Figs 13a–c). Apparent resistivity data at these sites range consistently between 10 and 50 Ωm for periods <5 s (symbols in Fig. 14c). The reason for this outcome of PT inversion is not completely clear, but we suspect it may be due to the proximity of the Pacific Ocean. If PT are combined with VTF data which are particularly sensitive to vertical conductivity contrasts, this bias is reduced (Fig. 13c) and impedance amplitudes are much better recovered (Figs 14c).

A couple of sites from the Parkfield data set, however, are clearly affected by strong galvanic distortion. An example is site 408, located in the northwestern survey area on profile 2 (Fig. 15b). At this site, diagonal impedances are large at short periods (<100 s) and their apparent resistivity curves appear intriguingly similar to the corresponding off-diagonal element. Yet, dimensionality parameters (PT beta values) indicate 1-D behaviour for these periods. The distortion becomes even more apparent when compared to data at adjacent sites 407 and 409, which are located approximately 10 km southwest and northeast (Figs 15a and c). At sites 407 and 409 diagonal apparent resistivity curves are small for periods <100 s. In addition, off-diagonal apparent resistivity curves are very similar at all three sites (Figs 15a–c), but those of site 408 are shifted upwards by half (*Zxy*) and one (*Zyx*) decades indicating that distortion contains a static shift component.

Closer inspection of the inversion models in the vicinity of site 408 suggests that this distortion results in an artificial structure extending to great depth. Fig. 15(d) shows that the 3-D inversion introduces a 10 km wide resistive zone (>200 Ωm) beneath site 408 which intersects the low-resistive (<10 Ωm) surface layer; a 7–9-km-thick part of Earth's crust is affected. In contrast, inverting PT and/or VTF data yields a continuous surface conductive layer in this area (Figs 15e–f). The PT results are consistent with the data set as they reproduce both phases and shape of the apparent resistivity curves at site 408 and neighbouring stations (blue lines in Figs 15a–c). In addition, PT results are consistent with MT data dimensionality parameters which indicate 1-D subsurface structures for periods <100 s at sites in the northwestern survey area and geologic models where the San Joaquin valley is underlain by uniform sediments of the Great Valley sequence with thicknesses up to 12 km (Irwin 1990). Therefore, we conclude that the PT and PT + VTF inversion results are more reliable for this area. Where distortion is obviously large, data fit of PT inversion is usually better than that of impedance inversion in particular when inspected as phase tensor ellipses (lowermost panel in Fig. 15b). For the California data set such clear indications of significant galvanic distortion are limited to few sites.

5 DISCUSSION AND CONCLUSION

We have implemented phase tensor inversion in a widely used 3-D inversion code (ModEM), and tested this new capability with synthetic and real world data sets. Phase tensors by themselves have little information about absolute resistivity levels. Thus, consistent with the results of Patro *et al.* (2013), we find that PT inversion results depend strongly on the resistivity level of the prior model required by ModEM. However, tests with synthetic data confirm that inversion of PT data can recover the correct resistivity structure with sufficiently dense site spacing. For regional scale structures inversion results are most accurate if the prior model resistivity is close to the regional average of the subsurface. Our results suggest that appropriate prior model resistivities might be obtained by examining how NLCG iterations decrease for a range of starting model resistivity distributions and/or data types, which contain information about absolute resistivities such as impedances and apparent resistivities (Fig. 7). In fact, situations in which we have no knowledge of background resistivity at all are rare. After all, we do have MT survey data on hand, and can likely get some rough idea from looking at (or even inverting) 'average' impedances to narrow the range of suitable prior models.

An important new result of this study is that compared to PT-only inversion, joint interpretation of PT and VTF data consistently resulted in a better recovery of the absolute resistivity structure for both synthetic and real world data. Although both parameters contain information on relative changes of resistivity, PT data are more indicative of vertical contrasts, whereas VTF data are particularly sensitive to lateral variations. Thus, PT and VTF data complement each other, and in combination provide superior resolution. The effect was less pronounced for the synthetic OC example than for the Parkfield data set, where VTF data contributed significantly to recovery of the high resistivities at depth and in coastal areas. We surmise that the simple OC structure is already quite well constrained by one single data type so that integration of VTF data did not result in a similarly strong improvement.

Where MT data are affected significantly by galvanic distortion, impedance inversion without consideration of the distortion may fail to recover a meaningful subsurface model. In impedance inversion models of the synthetically distorted OC data set 'surface' artificial structures appeared extending down to approximately 5 km. The artefacts interfered with the recovery of the top of the conductive

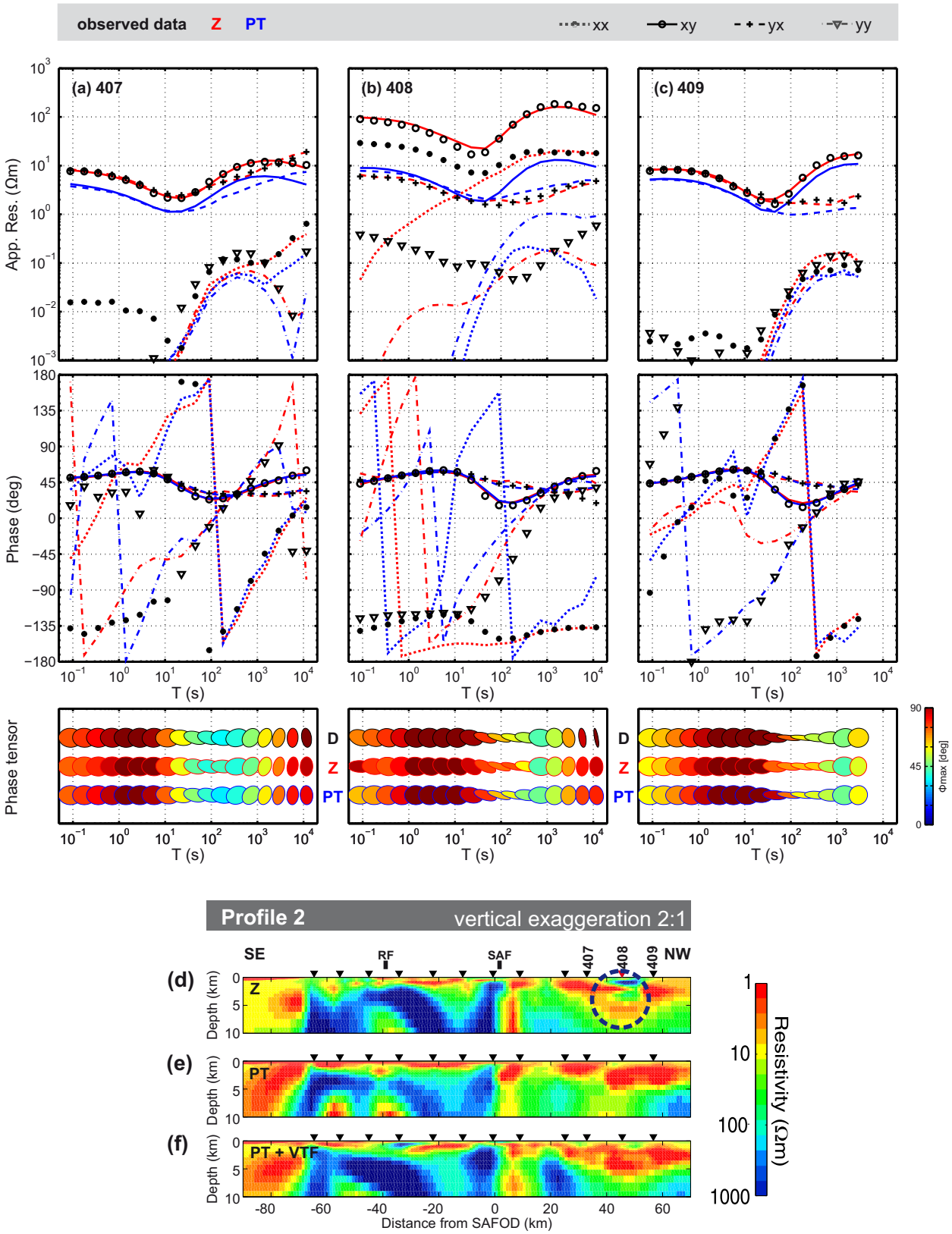

Figure 15. Galvanic distortion in the California MT data set and its effect on 3-D inversion results. (a)–(c) Observed (symbols) and modelled (lines) data at three adjacent sites located on profile 2; corresponding inversion models are shown in Figs 11a (Z) and e (PT). Site 408 (b) is strongly affected by galvanic distortion. Lowermost panels show normalized phase tensors; colour indicates maximum phase value. (d)–(f) The upper 10 km of the 3-D inversion models of Figs 11(a), (e) and (f) along profile 2. (d) The dashed black circle outlines artificial structures which appear in the models because site 408 is severely distorted. If not properly accounted for, this can cause large scale and deep reaching distortion of the 3-D inversion results. (e–f) 3-D inversion of PT (e) or joint inversion of PT + VTF data (f), which are both unaffected by local galvanic distortions, yields a smoother image, more consistent with the surrounding sites.

block at 2.56 km depth. PT inversion of the same data set yielded a clearer image of the subsurface. Our simulation may represent a severe case of galvanically distorted MT data, and impedance inversion is also challenged by the relatively coarse model mesh used. While fine model discretization and lower smoothing can reduce the influence of surface artefacts, mesh sizes are usually required to be kept small due to memory and/or run time limitations. In such cases, PT inversion can be particularly advantageous.

As the Parkfield MT data set is only mildly affected by galvanic distortion, deep structures (>10 km depth) are generally similarly imaged by PT and impedance inversion models. However, PT and joint PT + VTF inversion could improve recovery of the sedimentary sequences of the San Joaquin valley where we can expect fairly homogenous structures in the upper 10 km. With the joint PT + VTF inversion, we could identify artefacts introduced into models due to galvanic distortion.

In short, PT inversion is applicable to real-world data sets and proved to be advantageous in the presence of galvanic distortion. Sensible setup of prior (and starting) model resistivities which incorporates available *a priori* knowledge is essential to recover a reliable subsurface model. In regions featuring strong resistivity contrasts and a wide range of resistivities, this can be challenging. The most promising results were obtained with a joint inversion of PT and VTF data, which facilitated recovery of the true subsurface resistivities in particular for regions with resistivities far off the starting/prior model. Nevertheless, to obtain a comprehensive image of the subsurface with respect to both resistivity structure and absolute resistivities, PT, VTF and impedance inversion results should be compared and combined to exploit the advantages of each data type and to achieve a best possible interpretation.

ACKNOWLEDGEMENTS

Naser Meqbel and Anna Kelbert are acknowledged for helpful comments and discussions. We thank two anonymous reviewers for elaborate comments which improved the manuscript substantially. The instruments for the experiments were provided by the Geophysical Instrument Pool Potsdam (GIPP). The field campaigns were funded by the Deutsche Forschungsgemeinschaft (DFG) and the German Research Centre for Geosciences Potsdam (GFZ). This work was funded by the Deutsche Forschungsgemeinschaft (Ri 1127/2, 4). GDE was supported by National Science Foundation Grant EAR1225496.

REFERENCES

Árnason, K., Eysteinsson, H. & Hersir, G.P., 2010. Joint 1-D inversion of TEM and MT data and 3-D inversion of MT data in the Hengill area, SW Iceland, *Geothermics,* **39,** 13–34.

Aster, R.C., Borchers, B. & Thurber, C.H., 2011. *Parameter Estimation and Inverse Problems,* Academic Press.

Avdeeva, A., Moorkamp, M., Avdeev, D., Jegen, M. & Miensopust, M., 2015. Three-dimensional inversion of magnetotelluric impedance tensor data and full distortion matrix, *Geophys. J. Int.,* **202**(1), 464–481.

Bahr, K., 1988. Interpretation of the magnetotelluric impedance tensor: regional induction and local telluric distortion, *J. Geophys.,* **62,** 119–127.

Becken, M., Ritter, O., Park, S.K., Bedrosian, P.A., Weckmann, U. & Weber, M., 2008. A deep crustal fluid channel into the San Andreas Fault system near Parkfield, California, *Geophys. J. Int.,* **173**(2), 718–732.

Becken, M., Ritter, O., Bedrosian, P.A. & Weckmann, U., 2011. Correlation between deep fluids, tremor and creep along the central San Andreas fault, *Nature,* **480,** 87–90.

Bibby, H.M., Caldwell, T.G. & Brown, C., 2005. Determinable and non-determinable parameters of galvanic distortion in magnetotellurics, *Geophys. J. Int.,* **163,** 915–930.

Booker, J., 2013. The magnetotelluric phase tensor: a critical review, *Surv. Geophys.,* **35**(1), 7–40.

Caldwell, T.G., Bibby, H.M. & Brown, C., 2004. The magnetotelluric phase tensor, *Geophys. J. Int.,* **158,** 457–469.

Cumming, W. & Mackie, R., 2010. Resistivity imaging of geothermal resources using 1-D, 2-D and 3-D MT inversion and TDEM static shift correction illustrated by a Glass Mountain case history, in *Proceedings World Geothermal Congress 2010,* Bali, Indonesia.

Egbert, G.D., 1997. Robust multiple-station magnetotelluric data processing, *Geophys. J. Int.,* **130,** 475–496.

Egbert, G.D. & Booker, J.R., 1986. Robust estimation of geomagnetic transfer functions, *Geophys. J. R. astr. Soc.,* **87,** 173–194.

Egbert, G.D. & Kelbert, A., 2012. Computational recipes for electromagnetic inverse problems, *Geophys. J. Int.,* **189**(1), 251–267.

Farquharson, C.G. & Craven, J.A., 2009. Three-dimensional inversion of magnetotelluric data for mineral exploration: an example from the McArthur River uranium deposit, Saskatchewan, Canada, *J. appl. Geophys.,* **68,** 450–458.

Heise, W., Caldwell, T.G., Bibby, H.M. & Bannister, S.C., 2008. Three-dimensional modelling of magnetotelluric data from the Rotokawa geothermal field, Taupo Volcanic Zone, New Zealand, *Geophys. J. Int.,* **173,** 740–750.

Heise, W., Caldwell, T.G., Bibby, H.M. & Bennie, S.L., 2010. Three-dimensional electrical resistivity image of magma beneath an active continental rift, Taupo Volcanic Zone, New Zealand, *Geophys. Res. Lett.,* **37,** L10301, doi:10.1029/2010GL043110.

Hill, G.J., Caldwell, T.G., Heise, W., Chertkoff, D.G., Bibby, H.M., Burgess, M.K., Cull, J.P. & Cas, R.A., 2009. Distribution of melt beneath Mount St Helens and Mount Adams inferred from magnetotelluric data, *Nat. Geosci.,* **2,** 785–789.

Ingham, M.R. *et al.*, 2009. A magnetotelluric study of Mount Ruapehu volcano, New Zealand, *Geophys. J. Int.,* **179,** 887–904.

Irwin, W.P., 1990. Geology and plate-tectonic development, in *The San Andreas fault system, California: U.S. Geological Survey Professional Paper,* Vol. 1515, pp. 61–80, U.S. Geological Survey.

Jiracek, G.R., 1990. Near-surface and topographic distortions in electromagnetic inductions, *Surv. Geophys.,* **11,** 163–203.

Jones, A.G., 2011. Three-dimensional galvanic distortion of three-dimensional regional conductivity structures: comment on three-dimensional joint inversion for magnetotelluric resistivity and static shift distributions in complex media by Yutaka Sasaki and Max A. Meju, *J. geophys. Res.,* **116,** B12104, doi:10.1029/2011JB008665.

Kelbert, A., Egbert, G.D. & deGroot Hedlin, C., 2012. Crust and upper mantle electrical conductivity beneath the Yellowstone Hotspot Track, *Geology,* **40**(5), 447–450.

Kelbert, A., Meqbel, N., Egbert, G.D. & Tandon, K., 2014. ModEM: a modular system for inversion of electromagnetic geophysical data, *Comput. Geosci.,* **66,** 40–53.

Koyama, T., 2009. Possibility of three-dimensional magnetotelluric (MT) inversion by using MT phase tensor data, in *Proceedings of the 11th Scientific Assembly of the International Association of Geomagnetism and Aeronomy IAGA,* 23–30 August 2009, Sopron, Hungary.

Ledo, J., 2006. 2-D versus 3-D magnetotelluric data interpretation, *Surv. Geophys.,* **27**(1), 111–148.

Meqbel, N., 2009. The electrical conductivity structure of the Dead Sea Basin derived from 2-D and 3-D inversion of magnetotelluric data, *PhD thesis,* Freie Universität Berlin, Berlin, Germany.

Meqbel, N.M., Egbert, G.D., Wannamaker, P.E., Kelbert, A. & Schultz, A., 2014. Deep electrical resistivity structure of the northwestern U.S. derived from 3-D inversion of USArray magnetotelluric data, *Earth planet. Sci. Lett.,* **402,** 290–304.

Nadeau, R.M. & Dolenc, D., 2005. Nonvolcanic tremors deep beneath the San Andreas Fault, *Science,* **307,** 389.

Newman, G.A., Gasperikova, E., Hoversten, G.M. & Wannamaker, P.E., 2008. Three-dimensional magnetotelluric characterization of the Coso geothermal field, *Geothermics,* **37,** 369–399.

Page, B.M., Thompson, G.A. & Coleman, R.G., 1998. Late Cenozoic tectonics of the central and southern Coast Ranges of California, *Bull. geol. Soc. Am.,* **110,** 846–876.

Patro, K.P., Uyeshima, M. & Siripunvaraporn, W., 2013. Three-dimensional inversion of magnetotelluric phase tensor data, *Geophys. J. Int.,* **192**(2), 58–66.

Ritter, O., Junge, A. & Dawes, G., 1998. New equipment and processing for magnetotelluric remote reference observations, *Geophys. J. Int.,* **132,** 535–548.

Rodi, W.L. & Mackie, R.L., 2012. The inverse problem, in *The Magnetotelluric Method: Theory and Practice,* chapter 8, pp. 347–414, eds Chave, A., Jones, A.G., Mackie, R.L. & Rodi, W.L., Cambridge Univ. Press.

Sasaki, Y., 2004. Three-dimensional inversion of static-shifted magnetotelluric data, *Earth, Planets Space,* **56,** 239–248.

Sasaki, Y. & Meju, M.A., 2006. Three-dimensional joint inversion for magnetotelluric resistivity and static shift distributions in complex media, *J. geophys. Res.,* **111,** B05101, doi:10.1029/2005JB004009.

Shelly, D.R., Ellsworth, W.L., Ryberg, T., Haberland, C., Fuis, G.S., Murphy, J., Nadeau, R.M. & Burgmann, R., 2009. Precise location of San Andreas Fault tremors near Cholame, California using seismometer clusters: slip on the deep extension of the fault, *Geophys. Res. Lett.,* **36,** L01303, doi:10.1029/2008GL036367.

Siripunvaraporn, W. & Egbert, G., 2000. An efficient data-subspace inversion method for 2-D magnetotelluric data, *Geophysics,* **65,** 791–803.

Siripunvaraporn, W. & Egbert, G., 2009. WSINV3DMT: vertical magnetic field transfer function inversion and parallel implementation, *Phys. Earth planet. Inter.,* **173,** 317–329.

Siripunvaraporn, W., Egbert, G., Lenbury, Y. & Uyeshima, M., 2005. Three-dimensional magnetotelluric inversion: data-space method, *Phys. Earth planet. Inter.,* **150,** 3–14.

Tietze, K. & Ritter, O., 2013. 3-D magnetotelluric inversion in practice—the electrical conductivity structure of the San Andreas Fault in Central California, *Geophys. J. Int.,* **195,** 130–147.

Weckmann, U., Magunia, A. & Ritter, O., 2005. Effective noise separation for magnetotelluric single site data processing using a frequency domain selection scheme, *Geophys. J. Int.,* **169,** 635–652.

Weckmann, U., Ritter, O., Chen, X., Tietze, K. & de Wit, M., 2012. Magnetotelluric image linked to surface geology across the Cape Fold Belt, South Africa, *Terra Nova,* **24**(3), 207–212.

Wheelock, B.D., 2012. Electromagnetic imaging of the crust and upper mantle of the central california continental margin, *PhD thesis,* University of California, San Diego, 272 pp.

Xiao, Q., Cai, X., Xu, X., Liang, G. & Zhang, B., 2010. Application of the 3-D magnetotelluric inversion code in a geologically complex area, *Geophys. Prospect.,* **58,** 1177–1192.

Zhang, H., Nadeau, R.M. & Toksoz, M.N., 2010. Locating nonvolcanic tremors beneath the San Andreas Fault using a station-pair double-difference location method, *Geophys. Res. Lett.,* **37,** L13304, doi:10.1029/2010GL043577.

APPENDIX

Each phase tensor element depends on six impedance tensor elements. According to the definition of the phase tensor (*cf.* eq. 2) Φ_{11} is given by

$$\Phi_{11} = \frac{X_{22}Y_{11} - X_{12}Y_{21}}{\det \mathbf{X}} = \frac{X_{22}Y_{11} - X_{12}Y_{21}}{X_{11}X_{22} - X_{21}X_{12}}.$$

The derivatives of Φ_{11} with respect to the eight components of $\mathbf{X}$ and $\mathbf{Y}$ are then:

$$\frac{\partial \Phi_{11}}{\partial X_{11}} = \frac{1}{(\det \mathbf{X})^2}\left[X_{22}\left(X_{22}Y_{11} - X_{12}Y_{21}\right)\right] = \frac{1}{\det \mathbf{X}} X_{22}\Phi_{11}$$

$$\frac{\partial \Phi_{11}}{\partial X_{12}} = \frac{1}{(\det \mathbf{X})^2}\left[-Y_{21}\det \mathbf{X} - X_{21}\left(X_{22}Y_{11} - X_{12}Y_{21}\right)\right]$$

$$= -\frac{1}{\det \mathbf{X}}\left(Y_{21} + X_{21}\Phi_{11}\right)$$

$$\frac{\partial \Phi_{11}}{\partial X_{21}} = \frac{1}{(\det \mathbf{X})^2}\left[-X_{12}\left(X_{22}Y_{11} - X_{12}Y_{21}\right)\right] = -\frac{1}{\det \mathbf{X}} X_{12}\Phi_{11}$$

$$\frac{\partial \Phi_{11}}{\partial X_{22}} = \frac{1}{(\det \mathbf{X})^2}\left[Y_{11}\det \mathbf{X} + X_{11}\left(X_{22}Y_{11} - X_{12}Y_{21}\right)\right]$$

$$= \frac{1}{\det \mathbf{X}}\left(Y_{11} + X_{11}\Phi_{11}\right)$$

$$\frac{\partial \Phi_{11}}{\partial Y_{11}} = \frac{1}{(\det \mathbf{X})^2}\left(X_{22}\det \mathbf{X}\right) = \frac{1}{\det \mathbf{X}} X_{22}$$

$$\frac{\partial \Phi_{11}}{\partial Y_{12}} = 0$$

$$\frac{\partial \Phi_{11}}{\partial Y_{21}} = \frac{1}{(\det \mathbf{X})^2}\left(-X_{12}\det \mathbf{X}\right) = -\frac{1}{\det \mathbf{X}} X_{12}$$

$$\frac{\partial \Phi_{11}}{\partial Y_{22}} = 0.$$

Similarly, derivatives for the other elements of the phase tensor can be derived.